Large-Eddy Simulations and Observations of Atmospheric Marine Boundary Layers above Nonequilibrium Surface Waves

PETER P. SULLIVAN

National Center for Atmospheric Research, Boulder, Colorado*

JAMES B. EDSON

Department of Marine Sciences, University of Connecticut, Groton, Connecticut

TIHOMIR HRISTOV

Department of Mechanical Engineering, The Johns Hopkins University, Baltimore, Maryland

JAMES C. MCWILLIAMS

Department of Atmospheric and Oceanic Sciences, and the Institute of Geophysics and Planetary Physics, University of California, Los Angeles, Los Angeles, California

(Manuscript received 16 February 2007, in final form 10 August 2007)

ABSTRACT

Winds and waves in marine boundary layers are often in an unsettled state when fast-running swell generated by distant storms propagates into local regions and modifies the overlying turbulent fields. A large-eddy simulation (LES) model with the capability to resolve a moving sinusoidal wave at its lower boundary is developed to investigate this low-wind/fast-wave regime. It is used to simulate idealized situations with wind following and opposing fast-propagating waves (swell), and stationary bumps. LES predicts momentum transfer from the ocean to the atmosphere for wind following swell, and this can greatly modify the turbulence production mechanism in the marine surface layer. In certain circumstances the generation of a low-level jet reduces the mean shear between the surface layer and the PBL top, resulting in a near collapse of turbulence in the PBL. When light winds oppose the propagating swell, turbulence levels increase over the depth of the boundary layer and the surface drag increases by a factor of 4 compared to a flat surface. The mean wind profile, turbulence variances, and vertical momentum flux are then dependent on the state of the wave field. The LES results are compared with measurements from the Coupled Boundary Layers Air–Sea Transfer (CBLAST) field campaign. A quadrant analysis of the momentum flux from CBLAST verifies a wave age dependence predicted by the LES solutions. The measured bulk drag coefficient C_D then depends on wind speed and wave state. In situations with light wind following swell, C_D is approximately 50% lower than values obtained from standard bulk parameterizations that have no sea state dependence. In extreme cases with light wind and persistent swell, $C_D < 0$.

1. Introduction

An outstanding question in wind–wave interaction studies is the effect of fast-running waves or swell on the winds and turbulence in the atmospheric planetary boundary layer (PBL). Swell-dominated wave fields occur after the passage of storm fronts, propagate long distances without significant dissipation (e.g., see estimates in Cohen and Belcher 1999), and often dominate the local wave-height variance. In this situation it is difficult to measure and isolate the contributions of locally generated wind waves to the surface roughness and stress. The impact of swell on surface drag parameterizations is a closely related question. Donelan and Pierson (1987) and Donelan et al. (1997) suggest that

* The National Center for Atmospheric Research is sponsored by the National Science Foundation.

Corresponding author address: Peter P. Sullivan, MMM Division, NCAR, Boulder, CO 80307-3000.
E-mail: pps@ucar.edu

DOI: 10.1175/2007JAS2427.1

swell influences are strong and that wind–swell alignment is an important factor for the measured drag coefficients (e.g., they report that the drag increases by a factor of 3 for swell opposing the wind). Thus, the surface stress likely depends on wind speed, wave age, and swell amplitude and direction.

In a pioneering study, Harris (1966) first reported the formation of a wave-driven wind in a laboratory wave tank. Since then a growing body of experimental evidence has documented unique marine surface-layer dynamics in the presence of swell: development of low-level jets (Holland et al. 1981; Miller 1999), positive upward momentum flux (Grachev and Fairall 2001; Smedman et al. 1994, 1999), mean velocity profiles decreasing with increasing height (e.g., Rutgersson et al. 2001), reduced turbulence levels (Drennan et al. 1999), and misalignment between surface stresses and mean winds (Grachev et al. 2003). Time series of surface-layer winds collected from the Research Platform *Floating Instrument Platform* (R/P *FLIP*), reported by Miller (1999, p. 122), clearly show the hourly transition from a logarithmic to nearly uniform, near-surface wind profile after a storm passage; coincident with the wind-profile change is a rapid reduction in the turbulent momentum flux. These features appear to be signatures of a wave-driven surface layer and invalidate the use of Monin–Obukhov similarity theory that often is used to predict air–sea fluxes (e.g., Rutgersson et al. 2001). The overall impact of swell throughout the PBL contradicts the common view that the depth of the wave boundary layer (WBL; i.e., the region directly impacted by waves) is quite shallow, $z < 3$ m (e.g., Makin and Mastenbroek 1996).

The goals of this study are to develop and use turbulence-resolving large-eddy simulations (LES) to improve the understanding of the interactions between atmospheric turbulence and surface waves, and to aid in the interpretation of observations from the Coupled Boundary Layers Air–Sea Transfer (CBLAST low wind) field campaign (Edson et al. 2007). Our use of LES to examine the low-wind/fast-wave regime in an atmospheric PBL is new (see Sullivan et al. 2004, 2006b) but we note that Reynolds-average closure models have previously been used to study some of the impacts of fast-moving waves on marine surface layers (e.g., Gent and Taylor 1976; Gent 1977; Li 1995; Kudryavtsev and Makin 2004). This LES study extends our previous direct numerical simulations over a wavy lower boundary (Sullivan et al. 2000; Sullivan and McWilliams 2002).

2. CBLAST field campaign

Motivation for the present investigation stems from observations collected in CBLAST and similar field studies; an overview of the CBLAST goals, measuring platforms, datasets, and preliminary analysis is given by Edson et al. (2007). CBLAST was a major field campaign designed to investigate boundary layer processes that couple the atmosphere, wave field, and ocean under a variety of low to moderate wind conditions. The site for CBLAST is the Atlantic Ocean south of Martha's Vineyard, Massachusetts, and intensive observation periods occurred in the summers of 2001 and 2003. The output from this field campaign is a large observational database gathered over multiple months using a variety of sensors and measuring platforms on both sides of the air–sea interface. One of the unique measuring platforms specifically developed for CBLAST is the Air–Sea Interaction Tower (ASIT) shown in Fig. 1. The ASIT is a low-profile, fixed structure that minimizes flow distortion and removes the need for motion correction. It is exposed to effectively infinite fetch for south-southwesterly wind directions. Atmospheric sensors at fixed heights and on a vertical profiler provided direct turbulence flux measurements, wind profiles, and surface wave information. For our purposes we use a small subset of the CBLAST data, focusing on the observations of the surface-layer winds and wave fields gathered from the ASIT.

Wind–wave equilibrium is the asymptotic state of aligned winds and waves where the wave spectrum is fully developed and the peak frequency and shape of the wave spectrum are only changing slowly with time; it occurs most often at moderate to high winds $U_a \geq 10$ m s^{-1}. A bulk measure of wind–wave equilibrium is when the ratio of the peak frequency (or peak phase speed C_p) of the wave-height spectrum to a reference atmospheric wind U_a attains a limiting value, $C_p/U_a \approx 1.2$ (e.g., Alves et al. 2003). The CBLAST observations strongly emphasize the nonequilibrium and variable nature of winds and waves at low winds. Edson et al. (2007) finds that the histogram of surface wind speed collected over many months exhibits a maximum between 4 and 6 m s^{-1}, with a few excursions up to 10 m s^{-1}, and with a highly preferred wind direction from the southwest, about 225° from north [see Figs. 4 and 5 from Edson et al. (2007)]. Figure 2 shows that the relative orientation between U_a and C_p, that is, the wind–wave angle ϕ, is nearly randomly distributed. The histogram of the wind–wave angle has a modest peak in the range of aligned winds and waves $-30° \leq \phi \leq 30°$ but crossing winds and waves, $\phi = \pm 90°$, and even opposing, $\phi = \pm 180°$, are equally probable. Given the observed preferred wind direction reported by Edson et al. (2007), the variability in ϕ must largely be a consequence of nonlocal wave components, that is, a result of remotely generated swell propagating into the ob-

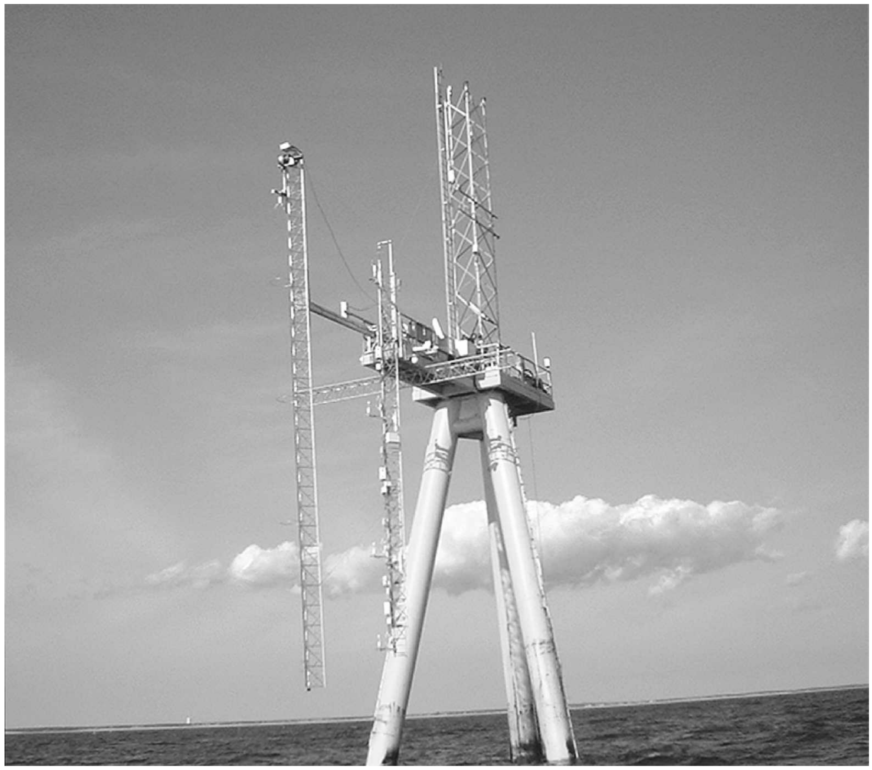

FIG. 1. The Air–Sea Interaction Tower with twin masts deployed during the CBLAST field campaign. Sonic anemometers mounted on the left (forward) mast translate vertically to obtain fine spatial resolution of the mean velocity and scalar profiles, while fixed sonic anemometers attached to the right (rearward) mast are used to measure vertical (turbulence) fluxes of momentum and scalars.

servation region. This conclusion is quantified by the histogram of the wave age parameter $C_p/U_a \cos\phi$ shown in Fig. 2.[1]

The CBLAST surface wind and wave fields are found to be dominated by relatively fast-moving waves (or old seas) $|C_p/U_a \cos\phi| > 1.2$. The likelihood of wave age lying outside the interval [0, 1.2] is about 75%. We note that some of the large wave age values are a consequence of crossing winds and waves when $\phi \approx \pm\pi/2$. The overall conclusion remains, however, that when the winds are light the wave field is most often in disequilibrium with the local winds. Churchill et al. (2006), using the method described by Hanson and Phillips (2001), provides a detailed description of the complex CBLAST wave fields.

Surface waves are the primary source of roughness

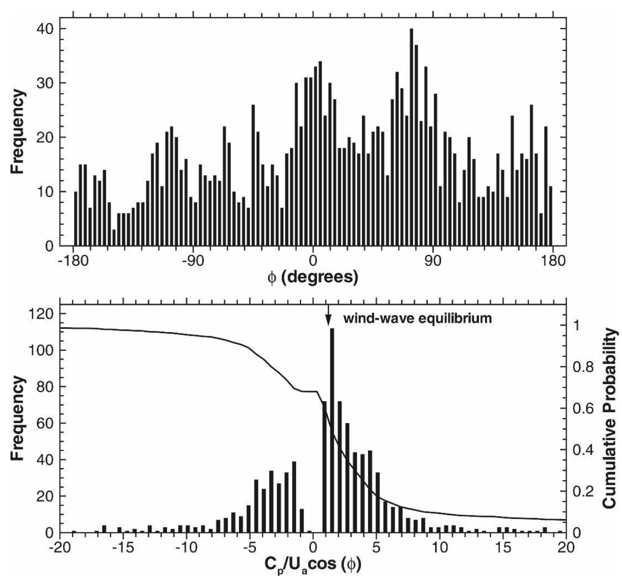

FIG. 2. Frequency histogram of (top) wind–wave angle ϕ and (bottom) wave age $C_p/U_a \cos\phi$ during CBLAST for all wind–wave conditions. In the bottom panel the solid line is the cumulative probability sum $1 - \int_0^x p(x')\,dx'$, where $p(x)$ is the probability density function.

[1] Several definitions of wave age are used in the literature (e.g., see Komen et al. 1994; Alves et al. 2003; Plant 1982). The present definition is adopted since it accounts for the directional alignment between winds and waves. In particular, the definition captures the variability in wave age and the occurrence of counterseas seen in our data.

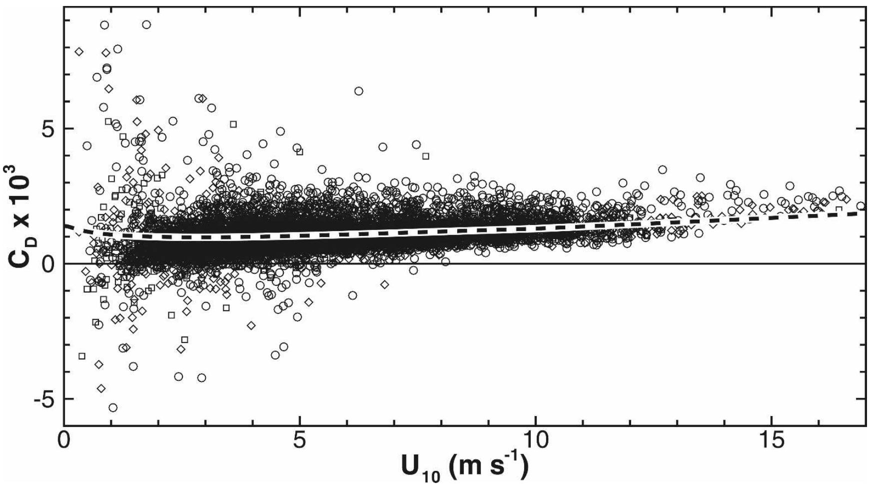

FIG. 3. Drag coefficients obtained from three measurement levels (squares, diamonds, circles) = (4.0, 6.0, 10.0) m during CBLAST (Edson et al. 2006); C_D is referenced to a 10-m height and neutral conditions. The TOGA COARE 3.0 parameterization is indicated by the dashed line. Note the negative values of C_D and increase in variability at low winds.

for the PBL, and it is a long-standing goal of marine surface-layer research to quantify the drag of the sea surface as a function of wind speed. Figure 3 shows the variation of the neutral drag coefficient C_D as function of the reference atmospheric wind speed U_a at a height $z = 10$ m (Edson et al. 2007). The results are from three different measurement heights along the ASIT gathered over the entire CBLAST observation period. The average C_D varies linearly with wind speed in close agreement with the Tropical Ocean and Global Atmosphere Coupled Ocean–Atmosphere Response Experiment (TOGA COARE) 3.0 parameterization (Fairall et al. 2003). However, notice the largest scatter in C_D is at low wind speed and that over certain periods, $C_D < 0$. We hypothesize some of this scatter is attributed to the nonequilibrium state of winds and waves at low winds shown in Fig. 2.

3. PBL wavy-surface problem formulation

The CBLAST observational results illustrate that in low to moderate winds the most common state of the marine boundary layer is disequilibrium between the surface-layer winds and the underlying wave field; usually the wave field is propagating faster than and at an angle to the mean surface wind. Our study is intended to elucidate the impact of nonequilibrium waves on turbulence in the low-wind atmospheric surface layer and more generally the PBL. To investigate this low-wind/fast-wave regime a large-eddy simulation model of the PBL with the ability to resolve moving sinusoidal modes at its lower boundary was developed. A description of the LES model including the governing equations, grid generation, and numerical method is provided in the appendix. This LES model is idealized, as a complete simulation of turbulent winds and a fully interacting wave field at all scales of interest is not computationally feasible. The design of our PBL wavy-surface numerical experiments instead focuses on formulating process studies to expose impacts of fast-moving waves on surface-layer winds.

Here we emphasize neutrally stratified (zero surface heat flux) PBLs where the wave propagation speed c is large compared to the surface wind and also when the waves are stationary, $c = 0$. Three regimes are considered, namely, wind following waves, wind opposing waves, and stationary bumps (or small hills). These cases serve to illustrate the importance of wave phase speed relative to wind speed (i.e., wave age) and the orientation of winds and waves.

In our LES experiments, the imposed surface wave is two-dimensional (i.e., has only x–z variations) with wavelength $\lambda = 100$ m, amplitude $a = 1.6$ m, low wave slope $2a\pi/\lambda = 0.1$, and propagates in either the positive or negative x direction. Based on the linear dispersion relationship $c^2 = g\lambda/2\pi$, the moving wave has phase speed $c = 12.5$ m s^{-1}. We set the surface roughness $z_o = 2 \times 10^{-4}$ m, a typical value for a low-wind marine boundary layer (Donelan 1998; Fig. 2). Essentially, the z_o parameterization accounts for the drag of unresolved small-scale waves riding on the larger-scale resolved swell. The geostrophic winds are $[(U_g, V_g) = (5, 0)]$ m s^{-1} and the surface heat flux $Q_* = 0$. Relatively shallow PBLs are simulated with an initial depth $z_i = 400$ m.

TABLE 1. Simulation properties.

Run name	U_g (m s^{-1})	Q_* (K m s^{-1})	ϕ (°)	C_D ($\times 10^3$)	Comments
ZN	5	0.0	6.8	1.2	Flat z_o surface, neutral flow
BN	5	0.0	19.0	3.7	Stationary bumps, neutral flow
FN	5	0.0	−2.3	−0.12	Wind following waves, neutral flow
FC	5	0.01	−2.1	−0.1	Wind following waves, slight convection
FN2	2	0.0	−6.1	−2.2	Wind following waves, neutral flow
ON	5	0.0	172.3	6.6	Wind opposing waves, neutral flow

The initial temperature sounding $\partial\overline{\theta}/\partial z = 0$ for $0 < z < z_i$, with a strong stable inversion where $\partial\overline{\theta}/\partial z = 0.01$ K m^{-1} above z_i. In all runs the Coriolis parameter $f = 10^{-4}$ s^{-1}. Thus our numerical experiments are an idealization of a near-neutral PBL above remotely generated swell with light winds as the LES wave age parameter $c/U_g > 2$.

To explore the sensitivity of the LES solutions we also compare flows where we add a small amount of surface heating $Q_* = 0.01$ K m s^{-1}, set the wave amplitude $a = 0$ to generate a traditional flat z_o-surface PBL, and reduce the geostrophic wind $(U_g, V_g) = (2, 0)$ m s^{-1}. A summary of the LES experiments discussed here is provided in Table 1. For easy identification the table includes an abbreviated run name with comments describing the bulk condition of the simulation, for example, case FN is a simulation with wind following waves and neutral stratification ($Q_* = 0$). Also in this table, ϕ is the angle between the wave propagation direction and the surface wind, and C_D is the drag coefficient deduced from the LES data at $z = 15$ m. Other parameters in Table 1 are as defined above.

For the suite of LES experiments, the computational domain (1200, 1200, 800) m is discretized using (250, 250, 96) grid points with the horizontal resolution nearly constant in physical space $(\Delta x, \Delta y) \approx (4.8, 4.8)$ m. As a result of the horizontal mesh, the waveforms imposed at the lower boundary are well resolved, approximately 25 grid points per wave. In x–z planes a conformal surface-fitted mesh is constructed between the surface wave $z_b = h(x, t) = a \cos [k(x - ct)]$ and the horizontally flat top of the computational domain $z = z_L$ (see the appendix and Fig. 4). The vertical spacing is varied in order to capture the different scales of motion in the PBL; tight spacing $\Delta z \approx 1$ m is used near the surface, and the spacing expands smoothly with $\Delta z \approx 14$ m at z_i, to $\Delta z \approx 28$ m well above the PBL at the top of the computational domain. Approximately 75 grid levels are located between the surface and the PBL inversion. Within the PBL the grid aspect ratio $\Delta x/\Delta z$ varies from about 4.8 at the surface to about 0.34 at the PBL inversion. At the surface the mesh aspect ratio is just within the acceptable limits for anisotropic LES grids (Scotti et al. 1993). The LES are computationally intensive. The time step is limited by the Courant–Fredrichs–Lewy (CFL) condition based on the speed of the wave c and the fine horizontal spacing Δx; typical time steps are $\Delta t \leq 0.23$ s. To obtain statistically stationary solutions for these shear-dominated flows requires about 200 000 time steps. Statistics are obtained by combined spatial and temporal averaging over the last 3–4 h of the simulations. To reduce the computa-

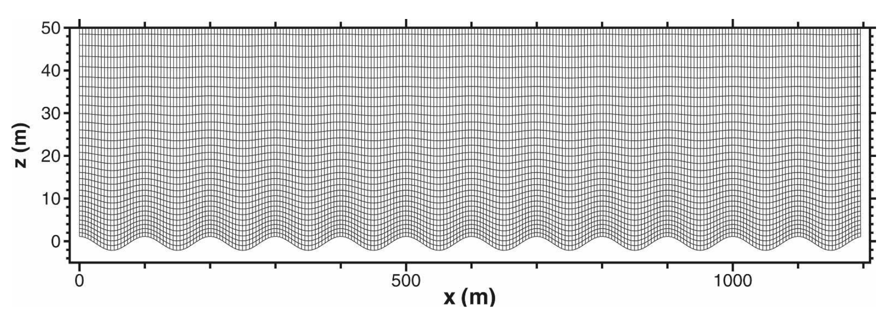

FIG. 4. An x–z slice of the conformal mesh in the lowest 50 m used in the LES of turbulent flow over water waves. The amplitude of the wave $a = 1.6$ m and the entire computational domain is $(x_L, y_L, z_L) = (1200, 1200, 800)$ m. The cell aspect ratio is distorted by the plotting scales. In the computational coordinates (ξ, η, ζ), surfaces of constant ζ, i.e., ξ–η planes, follow the underlying wavy shape at $\zeta = 0$ and smoothly blend into x–y planes as ζ increases away from the boundary.

tional costs many of the simulations are created from an initial seed run containing fully developed turbulence. The computational burden is further increased by the iterative pressure solution (see the appendix), which increases the cost of the present simulations by a factor of 2 compared to LES over a flat surface with no resolved surface undulations.

4. LES results

Coupling of the wind fields to the underlying wavy surface is found in instantaneous fields (see section 4a) and also in low-order statistical moments (see section 4b). To interpret these results it is helpful to first present the ensemble average equations of motion above an imposed wave. The LES equations for the resolved Cartesian velocity components $\overline{\mathbf{u}} = (\overline{u}, \overline{v}, \overline{w})$, where the overbar indicates spatial filtering, are formulated in surface-fitted wave-following coordinates (ξ, η, ζ) [see (A12) in the appendix and Fig. 4]. In these coordinates and in a frame of reference moving with the wave speed c, the ensemble average momentum equations for mean $\langle \overline{u}, \overline{v} \rangle$ in the horizontally homogeneous limit are

$$\frac{\partial}{\partial t}\left\langle \frac{\overline{u}}{J} \right\rangle + \frac{\partial}{\partial \zeta}\left\langle W\overline{u} + \tau_{11}\frac{\zeta_x}{J} + \tau_{13}\frac{\zeta_z}{J} + p^*\frac{\zeta_x}{J} \right\rangle = f\left\langle \frac{\overline{v} - V_g}{J} \right\rangle, \tag{1a}$$

$$\frac{\partial}{\partial t}\left\langle \frac{\overline{v}}{J} \right\rangle + \frac{\partial}{\partial \zeta}\left\langle W\overline{v} + \tau_{12}\frac{\zeta_x}{J} + \tau_{23}\frac{\zeta_z}{J} \right\rangle = f\left\langle \frac{U_g - \overline{u}}{J} \right\rangle, \tag{1b}$$

where we have assumed the special situation of a 2D surface wave. In (1), W is the contravariant flux velocity normal to a ζ surface, $p^* = \overline{p}/\rho_o + 2e/3$ is the pressure, τ_{ij} are subgrid-scale momentum fluxes, $e = \tau_{ii}/2$ is the subgrid-scale energy, ρ_o is a reference air density, f is the Coriolis parameter, (ζ_x, ζ_z) are grid metrics, and J is the Jacobian of the grid transformation. Also, angled brackets $\langle\cdot\rangle$ denote a spatial average over (ξ, η) coordinates along lines of constant ζ. For steady flow the mean Ekman motions following a wavy surface result from the force balance between vertical divergence of total (vertical) momentum flux and geostrophic pressure gradients ($-f\ V_g$, $f\ U_g$, 0). The momentum flux terms that appear on the left-hand side of these equations contract to their common form for a PBL above a flat uniform surface (e.g., Garratt 1992) when the computational ξ gridlines tend to flat surfaces in physical space. As shown in Fig. 4, near the surface the mesh oscillates with the underlying wave but the computational coordinates (ξ, ζ) are generally aligned with the Cartesian coordinates (x, z). Above $z \sim 50$ m the horizontal gridlines are effectively level and then $\xi_i \rightarrow x_i$, $\zeta_x/J \rightarrow 0$ so that $W \rightarrow \overline{w}$. Note at $\zeta = 0$, the wavy PBL Ekman Eqs. (1) contain an explicit contribution from the pressure distribution along the wave $p^*\ \zeta_x/J = -p^*\ z_\xi$. This term accounts for the resolved form stress (i.e., the drag or thrust) of the underlying wave (e.g., Sullivan et al. 2000). As discussed below, the sign of the surface form stress depends on the wind–wave orientation and wave age.

We note ensemble statistics can also be obtained at constant z by first interpolating the wave-following computational results to level z planes and then averaging. This mimics the observational approach to gathering statistics. Similar results are obtained from the two approaches at the same nominal z height (Sullivan et al. 2000). However, results in a constant z coordinate system do not provide information about flow dynamics between and below wave crests.

a. Flow visualization

Extensive visualization of the LES solutions highlights the impact of moving and stationary waves on surface-layer flow dynamics, and more broadly, on the overall PBL. The flow response to stationary bumps, wind following waves, and wind opposing waves is radically different as illustrated in Figs. 5 and 6. Inspection of the snapshots (Fig. 5) shows an unexpected coupling between the horizontal winds and waves in the situation with wind following waves (wave age $c/U_g \approx 2.5$). In this case a coherent pattern of accelerated winds greater than U_g occurs in the region above each wave trough, for $5 < z < 25$ m; the fastest local winds occur at $z \approx 15$ m above the mean water level and the u winds are slowest over the wave crests. The formation and coherence of a near-surface wind maximum (or supergeostrophic jet) in this neutrally stratified flow results from the coupling with fast-moving surface waves and not from the interaction between turbulence and stable stratification as in a nocturnal boundary layer (e.g., Saiki et al. 2000; Beare et al. 2006). The spatial patterns of the surface-layer winds in the presence of bumps or waves opposing the wind are noticeably different. Overall the surface-layer winds in these two cases are slower by roughly a factor of 4 compared to the situation of wind following waves and are always weaker than the geostrophic wind. The slowest surface-layer winds occur in the wave troughs in case ON or on the windward face of the wave for case BN. The organization of the resolved vertical velocity $\overline{w}$, shown in Fig. 6, depends on the wind–wave orientation and wave age

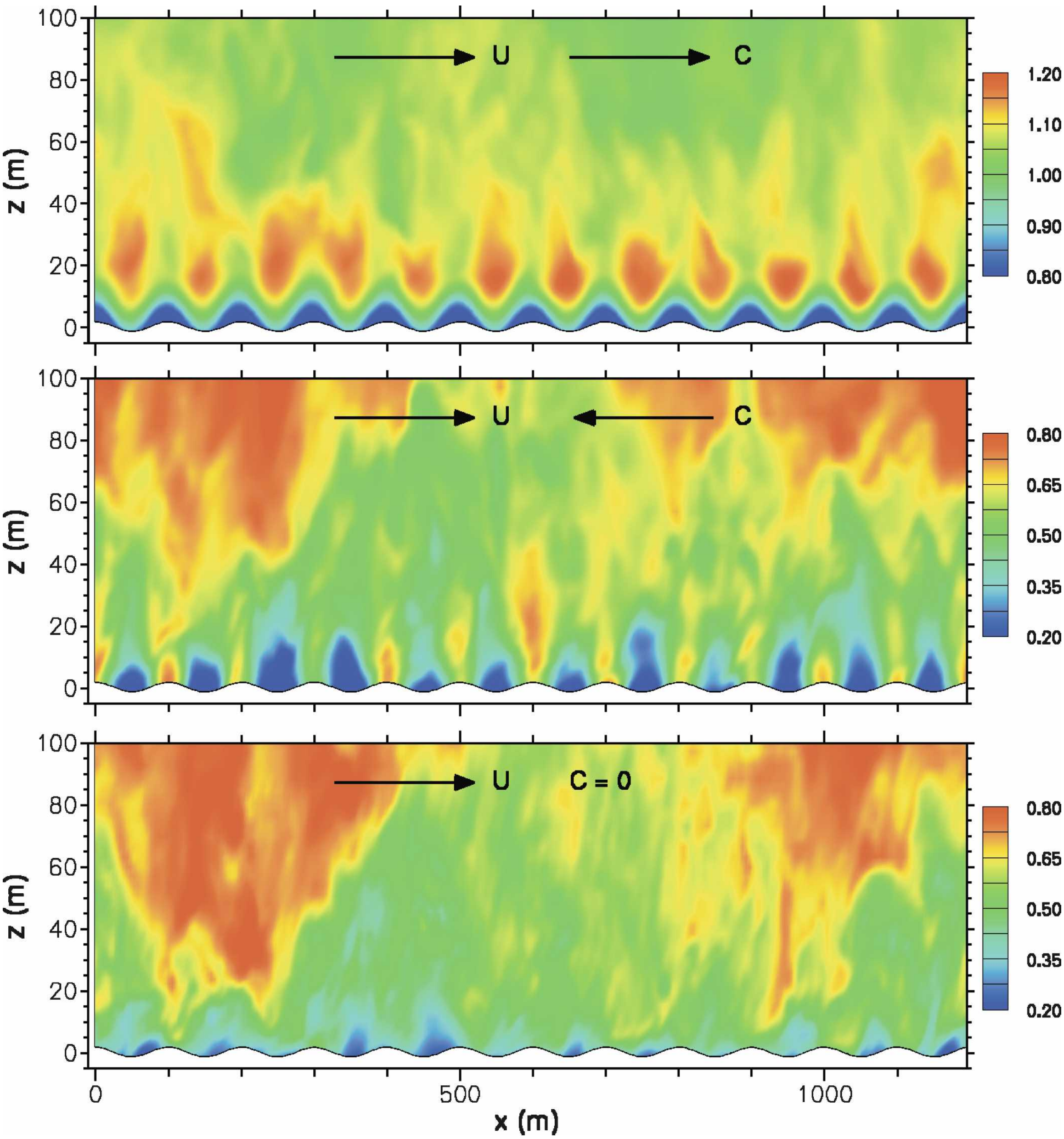

FIG. 5. Contours of the u component of the horizontal wind field for cases with moving and stationary surface waves. The nondimensional field shown is $\overline{u}/U_g$. (top) Wind following waves; (middle) wind opposing waves; and (bottom) stationary bumps. For each case the geostrophic wind $(U_g, V_g) = (5, 0)$ m s^{-1} and the wave slope $ak = 0.1$ where the wave amplitude $a = 1.6$ m. In the top and middle panels the wave phase speed $c = 12.5$ m s^{-1}. The color bar changes between the top and middle panels. Note the supergeostrophic winds near the surface in the top panel.

similar to the horizontal wind. For wind following waves, negative (positive) patches of $\overline{w}$ form upstream (downstream) of the wave crest. This pattern switches for wind opposing waves and stationary bumps. A comparison of cases FN, ON, and BN shows wave propagation enhances the coherence of the vertical velocity and alters the phase relationship between $(\overline{u}, \overline{w})$ compared to stationary bumps. This implies fast-moving waves can impact the distribution of vertical momentum flux as discussed in section 4b. We mention that the flow patterns (not shown) in the presence of high winds $U_g = 12.5$ m s^{-1}, which are representative of smaller wave age, are qualitatively similar to results for flow over stationary bumps (Sullivan et al. 2000).

Our interpretation of the cause of the u–w flow patterns in the surface layer is based on the structure of the

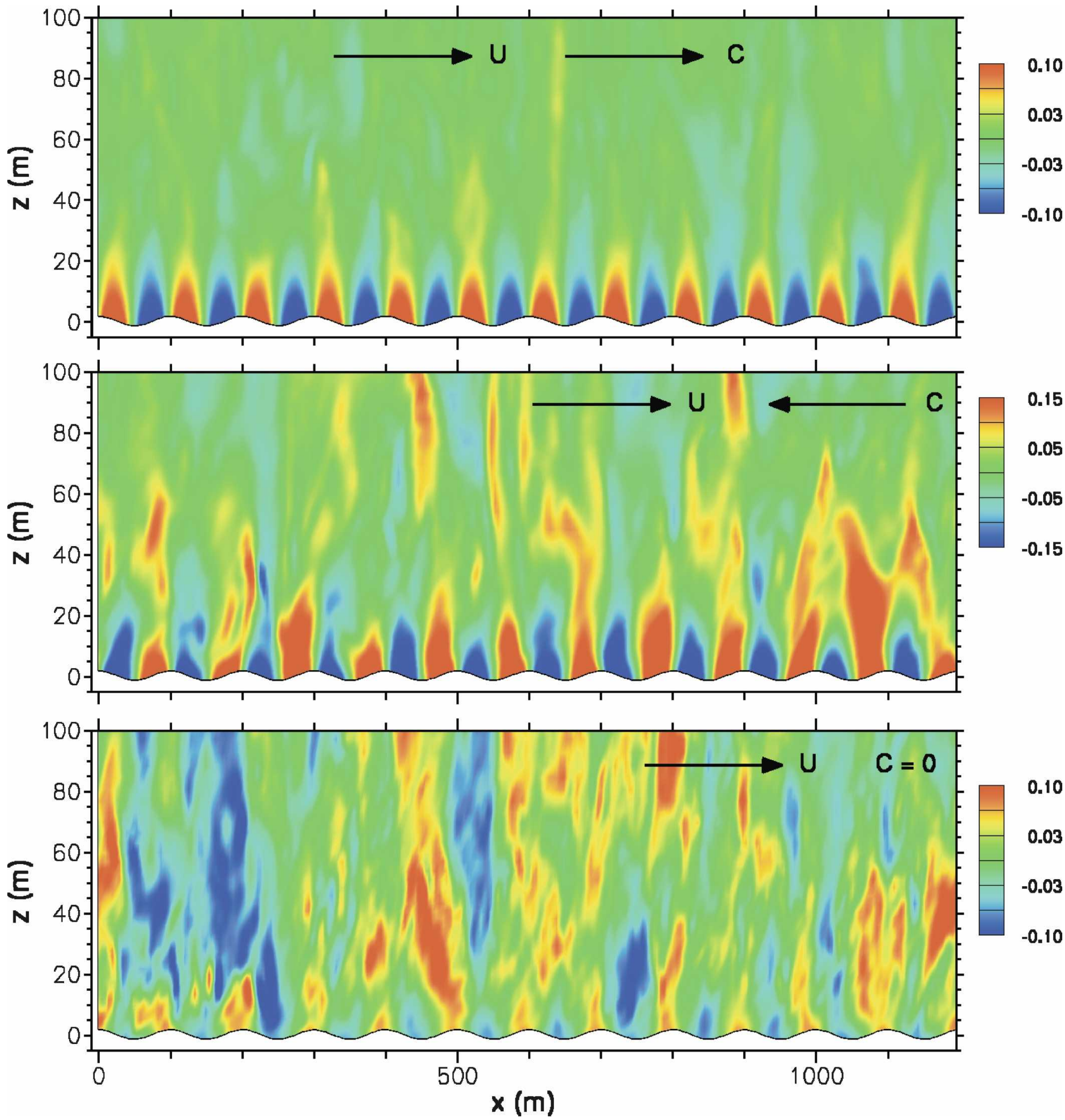

FIG. 6. Contours of the w component of the vertical wind field for cases with moving and stationary surface waves as in Fig. 5. The nondimensional field shown is $\overline{w}/U_g$. (top) Wind following waves; (middle) wind opposing waves; and (bottom) stationary bumps.

near-surface pressure field p^* shown in Figs. 7 and 8, and in particular the sign of the form stress (i.e., the surface drag) induced by the waves. In these plots we show the phase-averaged pressure signal $[p^*(x, z)] = \int_y p^*(x, y, z)dy/y_L$ normalized by U_g^2.[2] In the simulations a coherent pattern of positive and negative pressure correlated with the wave crests and troughs develops and extends well above the surface. Comparison of the three cases shows 1) the weakest pressure fluctuations occur in the case with wind following the waves; 2) wind opposing waves generates the most vigorous fluctuations, which can extend to a height of $2\pi z/\lambda > 2$; and 3) there is a subtle asymmetry in the pressure field relative to the underlying wave depending on the wave age and wind–wave orientation that leads to the form stress. In case FN, the negative pressure pattern is

[2] Our choice of normalization based on U_g instead of friction velocity u_* results from the observation that depending on wind–wave alignment and wave age the vertical momentum flux can change sign or vary appreciably with z in the surface layer, which leads to a poorly defined u_*.

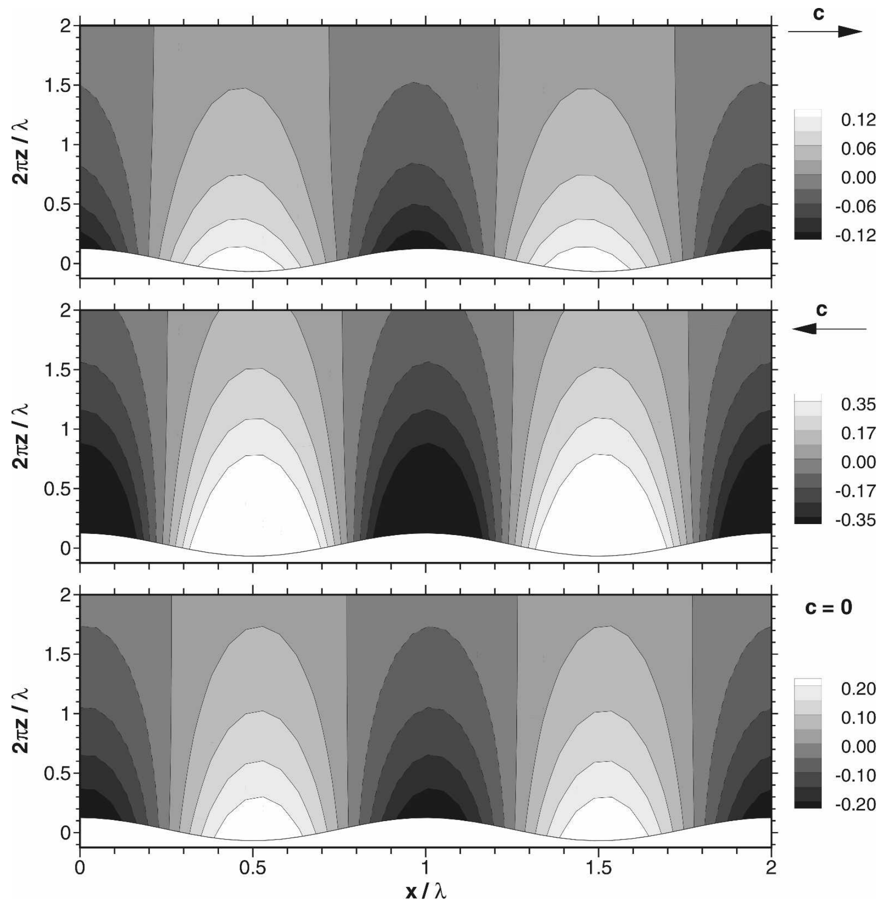

FIG. 7. Contours of the nondimensional and y-averaged pressure field $(p^*)/U_g^2$ close to the water surface for cases with moving and stationary waves. The winds are from left to right. Negative contours are indicated by dashed lines. (top) Wind following waves; (middle) wind opposing waves; and (bottom) stationary bumps. The vertical and horizontal coordinates are made dimensionless with the surface wavelength λ.

shifted slightly behind the wave crest ($x/\lambda < 1$); hence, the integration of the surface pressure over the wave acts in the positive x direction, implying a thrust on the winds. Meanwhile in cases ON and BN, the negative pressure minimum is shifted slightly ahead of the wave crest ($x/\lambda > 1$) and then the surface form stress acts as a drag on the surface winds as expected for stationary roughness. The magnitude and sign of the form stress reflects the change in character of the surface-layer turbulence.

The pattern of surface pressure in the case with wind following waves observed here in LES of a full PBL is qualitatively similar to the predictions from linear analysis (Belcher and Hunt 1998; Cohen and Belcher 1999), second-order closure (Gent 1977; Kudryavtsev and Makin 2004), and direct numerical simulations (Sullivan et al. 2000). All predict that for large values of wave age the form stress acts as a thrust on the winds;

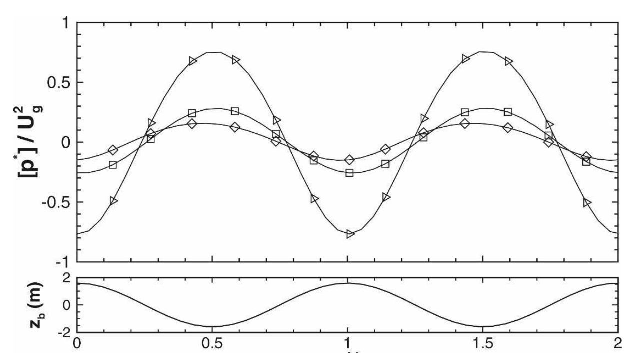

FIG. 8. Streamwise x variation of the nondimensional and y-averaged surface pressure for cases with moving and stationary surface waves. (bottom) The underlying wave. Here, diamonds indicate wind following waves, triangles indicate wind opposing waves, and squares indicate stationary bumps. The horizontal coordinate is made dimensionless by the wavelength λ.

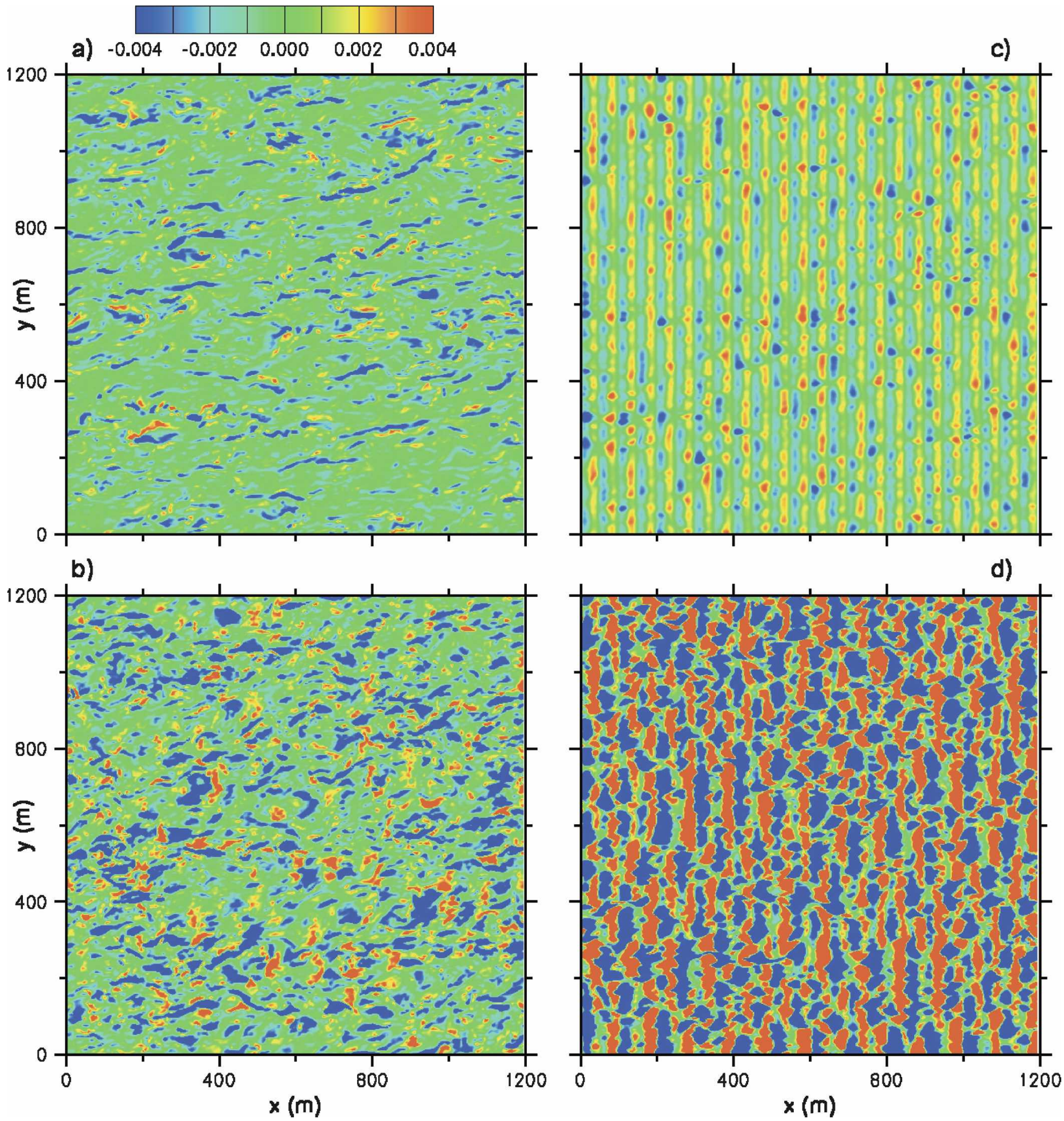

FIG. 9. Snapshot of the resolved vertical momentum flux $\overline{u}'\overline{w}'/U_g^2$ in an x–y plane at $z \approx 15$ m above the surface. (a) Flat z_o surface, (b) stationary bumps, (c) wind following waves, and (d) wind opposing waves. The wave and wind conditions are as described in Fig. 5.

this results from an asymmetrical pressure distribution with the minimum negative pressure forward of the wave crest.

Surface waves impact the instantaneous velocity and pressure fields, and thus we next examine how surface waves modulate the important momentum-flux-carrying coherent structures in the surface layer. The flow visualization in Fig. 9 compares the instantaneous (resolved) momentum flux $\overline{u}'\overline{w}'$ at a nominal height of $z = 15$ m (or $\zeta/z_i = 0.0375$) above different surfaces.[3] At this z the horizontal ξ gridlines are effectively level, and the momentum flux is dominated by resolved fluctuations. We observe over a flat z_o boundary the bulk of the negatively signed vertical momentum flux is carried by a few sparsely distributed structures aligned in the mean wind direction. Similar elon-

[3] Here $()'$ denotes a deviation from a horizontal average, that is, a turbulent fluctuation.

gated flux-carrying structures are observed in direct numerical simulations over a smooth wall (e.g., Adrian and Liu 2002), in other LES (e.g., Lin et al. 1996; Moeng and Sullivan 1994), and also in outdoor observations (e.g., Hommema and Adrian 2003). Fast-moving waves leading or opposing the wind destroy the coherence of these streaky near-wall structures. For wind following waves, the momentum flux structures in the surface layer are weak and carry slightly positive flux and impact the ensemble average profile (shown later in Fig. 11). The scale of the structures is observed to be linked to the horizontal scale of the waves. Changing the direction of wave propagation relative to the winds drastically alters the momentum flux patterns. Turbulent structures carrying large amounts of positive and negative momentum strongly correlated with the motion of the underlying waves are observed in Fig. 9d. Additional visualization shows that $\overline{u}'\overline{w}'$ induced by opposing waves remains coherent well above the surface layer and appears to interact with the background PBL turbulence. The structural features of the momentum flux in case ON are consistent with the velocity and pressure fields discussed previously. Wave age and wind–wave orientation are then clearly important for momentum flux generation since stationary bumps of the same amplitude as the moving waves considered here generate flux structures more comparable to those above a flat surface.

Animations of these and other LES solutions demonstrate that the structure of the velocity, pressure, and momentum flux fields are persistent in time and robust to reductions in surface roughness z_o and the presence of slight surface heating. As we illustrate later the impact of surface waves, especially in the case of wind following waves, is not confined to the surface layer but can extend over the PBL. In this case the mean shear is weak between the top of the surface-layer jet and z_i, which reduces turbulence production in the bulk of the PBL. Meanwhile the same wave moving in opposition to the wind acts as a large drag element slowing the surface-layer winds and generating vigorous turbulence that fills the PBL. The flow patterns found here in the presence of moving waves are in contrast to flow over a stationary hill (Belcher and Hunt 1998) and suggest propagating waves can in certain circumstances modify the overlying turbulent flow over the bulk of what is traditionally referred to as the PBL surface layer, corresponding to approximately $z_b < z < 0.1\ z_i$.

b. *Vertical profiles of winds, momentum fluxes, and variances*

Vertical profiles of the time- and space-averaged mean winds above a flat z_o surface, stationary bumps,

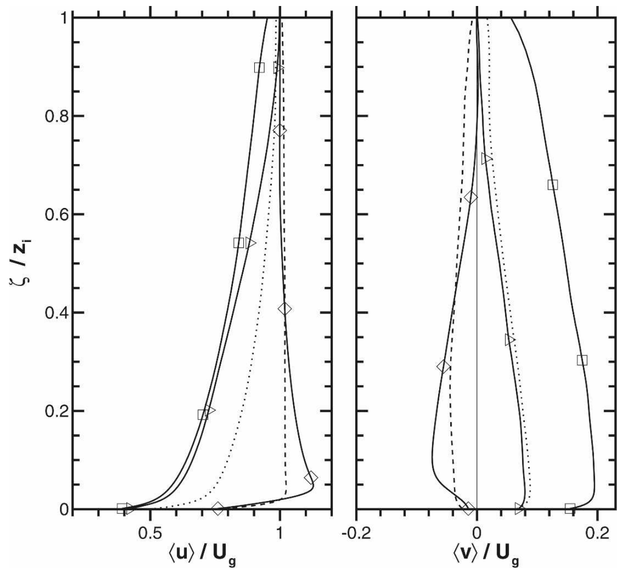

FIG. 10. Vertical profiles of the horizontal components of the mean wind $\langle\overline{u}\rangle$, $\langle\overline{v}\rangle$ for flow over waves. The spatial averaging is carried out along constant ζ surfaces, where ζ is the mean height above the wave. The nominal boundary layer depth z_i = 400 m. The cases are as follows: dotted line, no waves; squares, stationary bumps; diamonds, wind following waves; triangles, wind opposing waves; and dashed line, slight convection with wind following waves.

and moving waves are compared in Fig. 10. As anticipated based on the flow visualization in section 4a, the (u, v) wind profiles above stationary bumps and wind opposing waves are broadly similar to those above a flat z_o surface; the mean u profile is positively sheared over the entire PBL and stationary bumps and waves opposing the wind generate large mean vertical gradients. In the situation of wind following waves the structure of the mean wind profiles is radically different; the u wind profile exhibits a low-level jet $\langle\overline{u}\rangle/U_g > 1.1$ near $z \sim 20$ m and the sign of the v profile is switched compared to a flat surface. Above the low-level maximum the winds smoothly transition to the geostrophic wind with $\langle\overline{u}\rangle \approx U_g$ for $z \geq 200$ m. With small surface heating the low-level jet nearly disappears, $\langle\overline{u}\rangle \approx U_g$, and $\partial\langle\overline{u}\rangle/\partial z \approx 0$ over the bulk of the PBL, for 10 m $< z <$ 400 m. Hence in both the FN and FC cases the mean shear above the jet is either slightly negative or nearly zero. Below the height of the low-level maximum the u winds decrease sharply in order to match the surface boundary conditions. Because of the interaction with the wave field the horizontal wind direction depends on wave state. Given the orientation of the geostrophic wind, U_g parallel to the x direction, the surface winds at the standard reference height $z \sim 10$ m turn to the left as expected for flow over a flat z_o surface as $\langle\overline{v}\rangle > 0$. The degree of

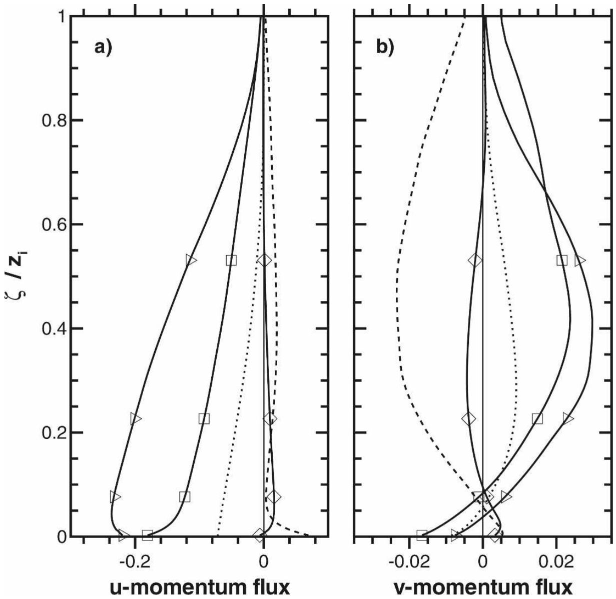

FIG. 11. Vertical profiles of the nondimensional vertical momentum flux for flow over waves. (a) The sum $\langle W\overline{u} + \tau_{11}\zeta_x/J + \tau_{13}\zeta_z/J + p^*\zeta_x/J\rangle \times 100/U_g^2$, and (b) the sum $\langle W\overline{v} + \tau_{12}\zeta_x/J + \tau_{23}\zeta_z/J\rangle \times 100/U_g^2$. The spatial averaging is carried out along constant ζ surfaces, where ζ is the mean height above the wave and z_i = 400 m. The cases are as follows: dotted line, no waves; squares, stationary bumps; diamonds, wind following waves; triangles, wind opposing waves; and dashed line, slight convection with wind following waves.

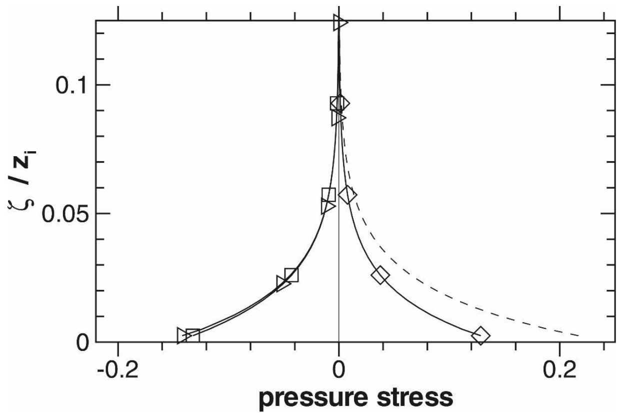

FIG. 12. Vertical profiles of the normalized pressure stress $\langle p^*\zeta_x/J\rangle \times 100/U_g^2$ near the water surface for flow over waves. The pressure is averaged along constant ζ surfaces with z_i = 400 m. The cases are as follows: squares, stationary bumps; diamonds, wind following waves; triangles, wind opposing waves; and dashed line, slight convection with wind following waves. Note for cases with wind following waves the waves impart a forward (positive) thrust on the winds.

turning increases for stationary bumps consistent with their larger surface form stress. However, an opposite trend is observed in the presence of wind following waves; the winds turn slightly to the right in the surface layer and $\langle\overline{v}\rangle < 0$, so that they are nearly aligned with the wave propagation direction. The rightward turning of the wind is a consequence of the Ekman balance for momentum above waves discussed below. This LES prediction is at least qualitatively similar to the observations in light winds above swell reported by Grachev et al. (2003).

Surface waves modify the momentum balance in the atmospheric PBL as shown in Figs. 11 and 12. In Fig. 11 the vertical distribution of the sum of flux contributions on the left hand side of the Ekman Eq. (1) is shown: in order, these terms are resolved momentum flux, subgrid-scale contributions, and pressure stress. In the cases with stationary bumps and wind opposing waves the distribution of the two components of the vertical momentum flux are as expected for a turbulent PBL above a rough surface; the dominant u momentum flux is negative with positive vertical divergence. Fast-moving waves leading the wind greatly alter the momentum flux distribution; the u component is slightly positive with negative vertical divergence while the sign and vertical divergence of the v component are opposite to their counterparts in a flat PBL. The cause of this unexpected behavior can be traced to the pressure stress variation shown in Fig. 12. At the wave surface, fast-moving waves impart a positive forward thrust on the winds opposite to that in flow over stationary bumps. In other words there is significant momentum transfer from the ocean to the atmosphere. The surface thrust from the waves is a large component of the momentum flux balance and acts counter to the usual drag induced by surface-generated turbulence. The vertical distribution of pressure stress above the surface $\zeta > 0$ is a consequence of formulating the Ekman flux budget (1) in wave-following coordinates. Its smooth monotonic variation with height shows that the surface asymmetry of the pressure contours with respect to the underlying wave field (see Fig. 7) persists with increasing distance z from the surface.

The variation and signs of both components of the momentum flux and mean winds are consistent with the formation of a low-level jet and are mandatory in order to achieve a steady balance between the pressure gradient forcing and momentum flux divergence. With wind following waves the Ekman balance of terms is opposite to that of a conventional PBL, the stress divergence serves to accelerate the u component of the wind while the pressure gradient acts to retard the flow. Finally, notice that with small amounts of convection the vertical u–momentum flux is small but clearly positive over the vertical extent 30 m $< z < z_i$. This is in contrast to a PBL over a land surface driven by shear

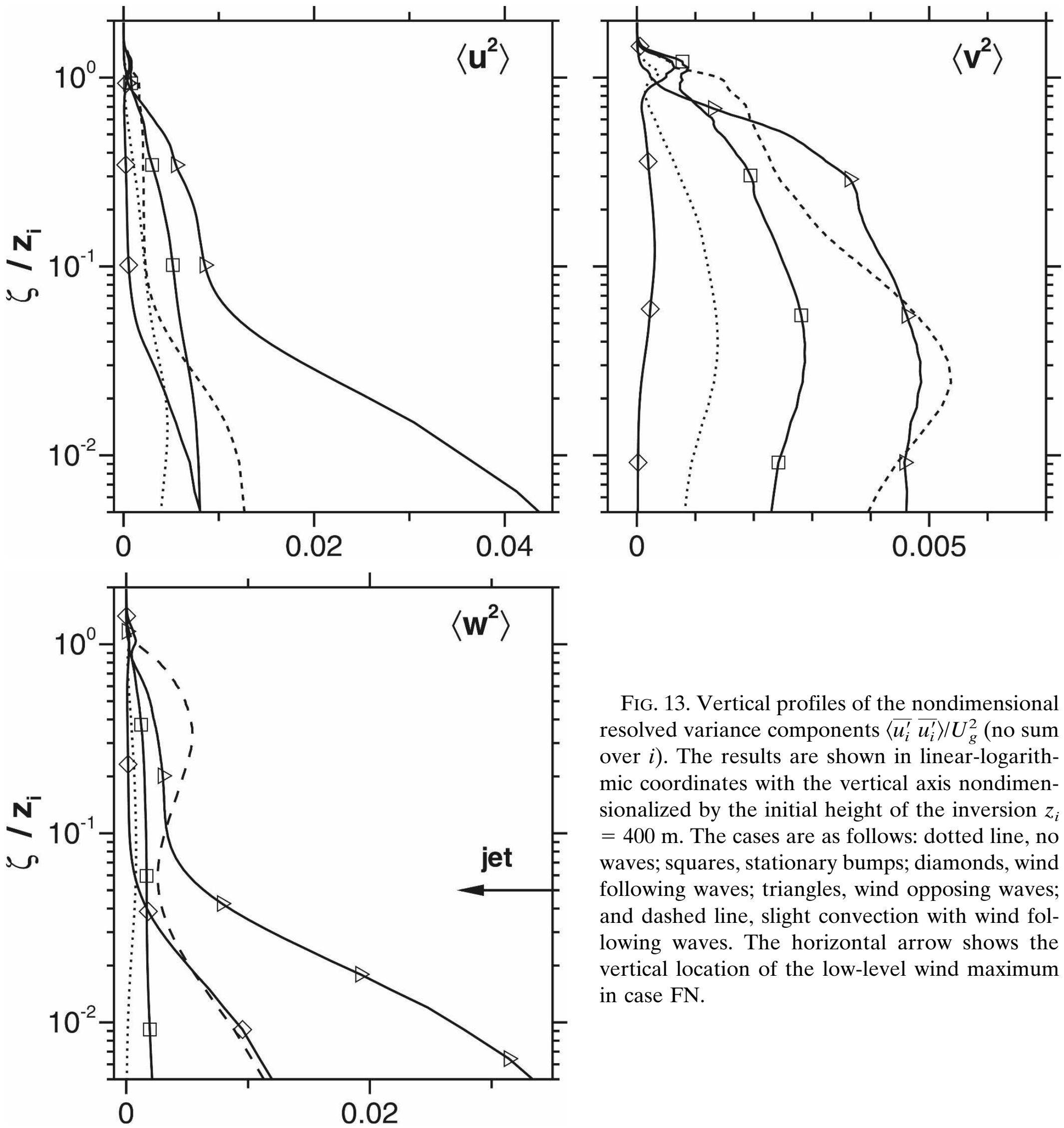

FIG. 13. Vertical profiles of the nondimensional resolved variance components $\langle \overline{u_i'}\,\overline{u_i'} \rangle / U_g^2$ (no sum over i). The results are shown in linear-logarithmic coordinates with the vertical axis nondimensionalized by the initial height of the inversion z_i = 400 m. The cases are as follows: dotted line, no waves; squares, stationary bumps; diamonds, wind following waves; triangles, wind opposing waves; and dashed line, slight convection with wind following waves. The horizontal arrow shows the vertical location of the low-level wind maximum in case FN.

and convection where the momentum flux in the upper PBL is negative (e.g., Moeng and Sullivan 1994). We speculate surface convection transports positive signed vertical momentum, generated by the wave field, to the upper regions of the PBL.

For a horizontally homogeneous PBL above a flat surface, the turbulent kinetic energy (TKE) budget (e.g., Moeng and Wyngaard 1989; Moeng and Sullivan 1994) contains two main sources of energy, namely, shear production $\mathcal{P} = -\langle \mathbf{u}'w' \rangle \cdot d\langle \mathbf{u} \rangle / dz$ and buoyancy $\mathcal{B} = g/\theta_o \langle w'\theta' \rangle$.[4] Here $\mathcal{P} > 0$ since $\langle \mathbf{u}'w' \rangle$ and $d\langle \mathbf{u} \rangle/dz$ are generally opposite in sign. In our shear-dominated PBLs the presence of surface waves alters the shear production mechanism and hence TKE. These changes are reflected in the (resolved) component variances $\langle \overline{u'}\,\overline{u'}, \overline{v'}\,\overline{v'}, \overline{w'}\,\overline{w'} \rangle$ shown in Fig. 13. Wave influences dominate near the surface but also impact the distribution of turbulence energy over the bulk of the PBL. In the neutral case, with wind following waves a near-surface velocity maximum is generated with slightly supergeostrophic winds $\langle \overline{u} \rangle / U_g \approx 1.1$ (see Fig. 10). As a result the shear between the surface wind maximum and the PBL top is near zero. Coupled with small vertical momentum fluxes (see Fig. 11), the shear production $\mathcal{P}$ is minimal over the bulk of the PBL. Note in Fig. 13 when $\zeta/z_i > 0.1$ the smallest variances occur in case FN. Swell propagating in the wind direction then has a significant impact on the turbulence level in the neutral

[4] In the definitions of $\mathcal{P}$ and $\mathcal{B}$ the $()'$ denotes a turbulent fluctuation and the fluctuating velocity vector $\mathbf{u}' = (u', v', w')$.

PBL as the modification of the turbulence production mechanism in the surface layer leads to a turbulence collapse in the overall PBL. Surface convection, however, still generates significant TKE in the PBL in the presence of waves as shown in Fig. 13. Stationary bumps and waves opposing the surface wind both generate turbulence variances larger than a neutrally stratified flat z_o surface consistent with their larger surface form drag and sheared mean wind profiles. Near the surface, $\zeta/z_i < 0.1$, and the (u, w) variances in the presence of moving waves are large due to the significant (irrotational) motion of the underlying wave field.

These LES predictions in the marine surface layer are qualitatively supported by the observations of Smedman et al. (1999) who find that turbulence production is significantly reduced in the presence of wind following waves. Thus TKE in the marine PBL depends on wind–wave orientation, wave age, and generally on the structure of the wave field.

5. Momentum fluxes from CBLAST and LES

Our LES results predict that the winds, turbulence fluxes, and variances as well as their mean profiles depend on bulk properties of the wave field, that is, wave age and wind–wave orientation. These computational results provide motivation to search for wave influences in measured wind fields from the CBLAST field campaign. Compared to real seas, the wave fields in the LES are highly idealized; for example, they do not include multicomponents, three-dimensionality, and time-varying wave amplitudes and phases. Hence, we expect wave influences to be more subtle and difficult to isolate in observations.

First we interrogate the CBLAST database searching for cases with winds and waves that conform to the LES idealizations for more detailed analysis. Based on a criterion of wind–wave angle $-30° < \phi < 30°$, approximately 100 periods of 60 min in duration are identified as cases of wind following waves. Unfortunately, numerous clean cases with waves directly opposing the winds are not present because of possible flow distortion from the ASIT superstructure (see Fig. 1). By expanding the wind–wave angle to $130° < \phi < 230°$ a limited number of cases are identified as wind opposing waves—just 18 periods of 20-min duration. In the data screening, no limits are placed on the range of atmospheric stratification, but we note that stable stratification is a potential source of variability (Smedman et al. 1997). For the selected cases with wind following waves shown in Fig. 14, the wave age $C_p/U_a\cos\phi$ spans a large range, approximately [1, 8]. This subset of the CBLAST data is dominated by fast-moving swell (or old seas)

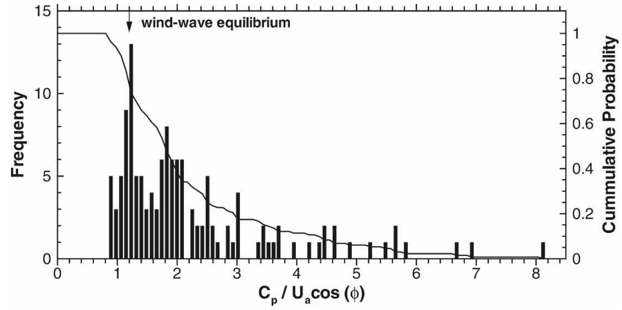

FIG. 14. Frequency of wave age for selected cases with wind following waves. The solid vertical bars show the frequency of occurrence and the solid line is the cumulative probability sum $1 - \int_0^x p(x')dx'$, where $p(x)$ is the probability density function.

with approximately a 75% probability of wave age greater than wind–wave equilibrium; the high probability of old seas in this subset of data is similar to that for the entire CBLAST dataset. Hence we expect wave influences are present in this subset of the CBLAST data.

LES predicts the surface-atmosphere momentum exchange depends on wave state. To expose and quantify this dependence in the CBLAST data a quadrant analysis of the observed vertical momentum flux is performed. This conditional sampling technique, first used with observational data by Chambers and Antonia (1981) and later by Smedman et al. (1999), separates the turbulent momentum flux $u'w'$ into four categories (quadrants) according to the sign of the two fluctuating velocity components as sketched in Fig. 15. In the surface layer of a rough wall boundary layer the net (average) momentum flux $\langle u'w'\rangle < 0$ and is dominated by sweeps and ejections associated with motions in quadrants Q2 and Q4. Positive flux contributions from the interaction quadrants Q1 and Q3 are less frequent and weaker in magnitude.

A quadrant analysis of the vertical momentum flux obtained in CBLAST and from our idealized LES data is displayed in Fig. 16. The CBLAST results for wind following waves are averages over the four vertical sonic positions $z = [4.0, 6.5, 10.0, 18.0]$ m and wave age bins of width equal to 0.09. In the cases with wind opposing waves, the observational results are only averaged over the four sonic positions owing to the limited dataset. For comparison we also display observational results for flow over stationary (terrestrial) roughness (Sullivan et al. 2003) and from Smedman et al. (1999) obtained at an independent marine site. The results are presented in terms of the normalized ratio of negative to positive momentum flux quadrants $Q_r = -(\mathrm{Q2} + \mathrm{Q4})/(\mathrm{Q1} + \mathrm{Q3})$ for varying wave age $C_p/U_a \cos\phi$. We find the quadrant ratio Q_r to be a robust statistical mea-

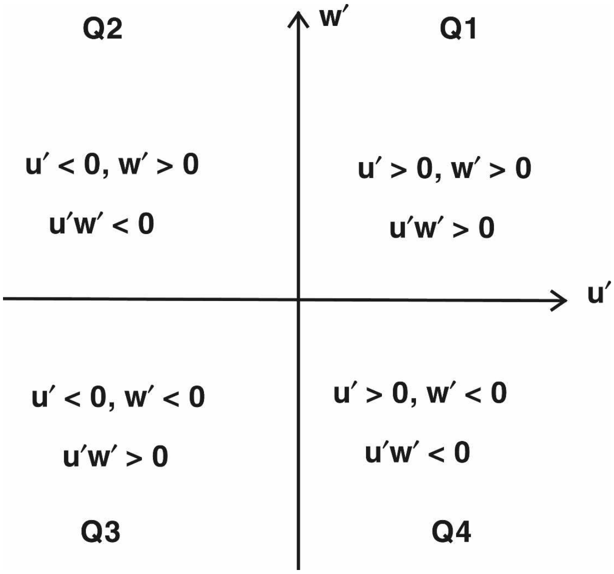

FIG. 15. Decomposition of the vertical momentum flux into quadrants (Q1, Q2, Q3, Q4) based on the sign of the fluctuating horizontal and vertical velocity (u', w').

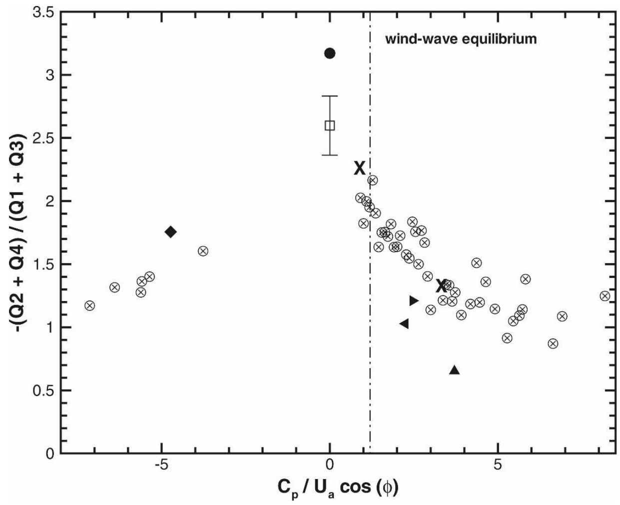

FIG. 16. Quadrant analysis of the vertical momentum flux in the marine surface layer for varying wave age with wind following and opposing waves. CBLAST results are indicated by crossed circles. For comparison we show observations of Smedman et al. (1999), denoted by X, and results for flow over stationary roughness (note wave age = 0) (Sullivan et al. 2003), indicated by an open square with an error bar. LES results at z ≈ 15 m above the surface are indicated by large filled symbols: circles, stationary bumps; diamonds, wind opposing waves (note wave age <0); left-pointing triangles, wind following waves; right-pointing triangles, wind following waves plus convection; and triangles, wind following waves for very light winds with $U_g = 2$ m s^{-1}.

sure that exposes the nature of the underlying surface, and in the present analysis brings out the wave dependence. The CBLAST results contain scatter but the quadrant flux ratio clearly contains wave influences, a distinct downward trend for increasing wave age $C_p/U_a \cos\phi > 1$. Our interpretation, based on the LES results, is that under low winds the fast-moving components of the wave field enhance the upward (positive) momentum transport from the ocean to the atmosphere and this momentum appears in the positively signed flux quadrants (Q1, Q3). At a sufficiently large wave age a near balance between negative and positive flux contributions is reached, implying zero surface drag. The quadrant momentum flux distributions are a consequence of competing effects; fast-moving waves generate positive momentum flux while small slow-moving waves act similar to conventional roughness elements. Also the effects of fast-moving waves on momentum transport are not confined to the first measurement level, $z = 4.0$ m, but extend over the bulk of the surface layer, up to at least $z = 18.0$ m, in agreement with the LES. The few observations reported by Smedman et al. (1999) also follow a similar trend with wave age as the CBLAST results. Notice Q_r appears to asymptotically approach a value measured at a rough land site for wave age approaching zero, that is, a field of young developing waves generates a distribution of momentum flux broadly similar to stationary roughness. Although Q_r provides information as to the distribution of momentum flux it does not provide scale information. Spectral analysis of surface-layer winds in the presence of waves (Drennan et al. 1999; Smedman et al. 2003) show that the low wavenumbers (or frequencies) are modified by swell, that is, for wind following waves.

The LES predictions for the distribution of vertical momentum flux are in general good agreement with the observational trends. They mimic the observed variation with wave age but likely overemphasize the wave-driven wind effects due to the highly idealized and persistent nature of the surface wave field. Thus LES predicts lower values of Q_r. Also, LES hints at an intriguing wave effect on the momentum flux for flows with wind opposing waves. Case ON with wave age −4.7 is characterized by high C_D (see Table 1), small surface wind speed, large momentum flux, and high variance. Opposing waves are efficient generators of fluctuation amplitude, which modulates the flux-carrying structures compared to a flat surface as shown in Fig. 9. This leads to a reduced value of Q_r in Fig. 16. The LES predictions for wind opposing waves are also verified by a limited number of CBLAST observations. The present LES results are further supported by independent direct numerical simulations of a wavy Couette flow (Sullivan et al. 2000).

Finally the wave influences observed in the vertical

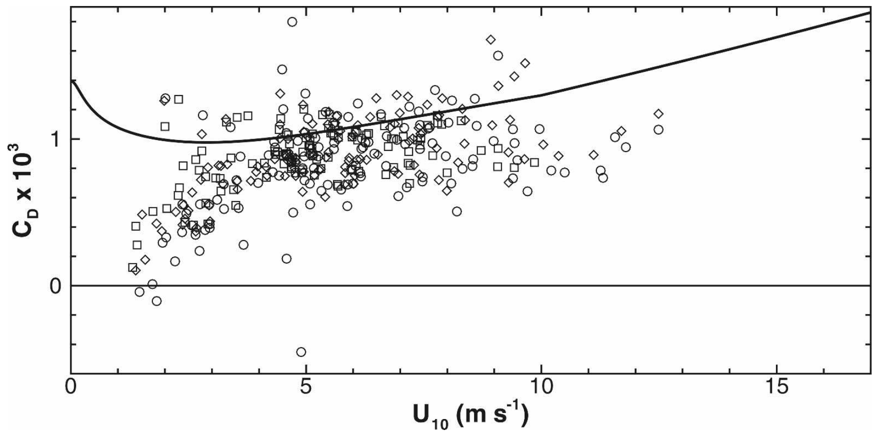

FIG. 17. The variation of the neutral drag coefficient with wind speed for wind following waves in CBLAST. The wave age for these observations is mostly greater than 1.2 as shown in Fig. 14. The vertical locations are nominally z = (4.0, squares; 6.5, diamonds; 10.0, circles) m. The TOGA COARE 3.0 parameterization is the solid line.

momentum flux naturally appear in the bulk measurement of the sea surface drag. Figure 17 shows the variation of the drag coefficient obtained in CBLAST for all cases with wind following waves. Again we emphasize that these results cover a range of sea state but are dominated by wave-age conditions greater than wind–wave equilibrium. Notice the majority of the C_D values fall well below the standard TOGA COARE parameterization especially at low wind speed. This effect is due to the presence of the underlying swell, which induces upward momentum transport from the ocean to the atmosphere as predicted by LES. In these cases the wave field alters the usual turbulence production mechanism in the marine surface layer and lowers the drag coefficient. Often the measured C_D is only 50% of the standard parameterization value and can clearly approach negative values. The values of C_D from the LES at z = 15 m, listed in Table 1, are at least qualitatively similar to the CBLAST measurements. Compared to a flat z_o-surface, fast-moving swell leading the surface wind leads to $C_D < 0$, while in the presence of opposing swell, C_D increases by more than a factor of 4 in agreement with the observations of Donelan et al. (1997).

6. Conclusions

Recent measurements from the Coupled Boundary Layers Air–Sea Transfer (CBLAST) field campaign (Edson et al. 2007) show that the winds and waves in the marine surface layer are frequently in a state of disequilibrium in light to moderate wind conditions where $U_a \leq 10$ m s^{-1}. Long-wavelength, fast-moving waves generated by distant storms often dominate the local wave-height variance and spectrum and propagate in arbitrary directions relative to the local wind. In terms of a bulk wave age $C_p/U_a \cos\phi$, where C_p is the phase speed of the peak in the wave-height spectrum and ϕ the wind–wave angle, the wave age is most often either negative or greater than the equilibrium value of 1.2. In low-wind conditions swell is then an important source of variability in measurements of the surface drag coefficient C_D.

To examine the interaction between atmospheric turbulence and swell, a large-eddy simulation (LES) model of the planetary boundary layer (PBL) is developed with the capability of imposing propagating sinusoidal modes at its lower boundary. The code is used to simulate a variety of PBLs with an emphasis on situations with wind following waves, wind opposing waves, and stationary bumps. The LES results illustrate the importance of wave phase speed relative to wind speed and the orientation of winds and waves. Surface-layer winds are modulated by the structure of the near-surface pressure field (i.e., the resolved surface form stress). In flow over stationary bumps or wind opposing waves, the resolved form stress is negative, while for wind following waves, the resolved form stress is positive. In the latter situation LES predicts momentum transfer from the ocean to the atmosphere and the generation of a low-level jet; the magnitude of the winds at $z \sim [10, 20]$ m are about 10% greater than the geostrophic wind and vary with surface heating. Our interpretation suggests that the jet formation results from a wave-induced turbulent momentum flux divergence that accelerates the flow and a retarding pressure gradient, both of which are opposite to the momentum balance in classical shear boundary layers. In a neutrally stratified PBL, the presence of a low-level jet reduces the mean shear between the surface layer and the PBL top, leading to a near collapse of turbulence in the PBL. The mean wind profile, turbulence variances, and vertical momentum flux are then dependent on the nature of the wave field, the wind–wave orientation, and wave age. The LES predictions for the dependence of vertical momentum flux on wave age are also found in the CBLAST observations. The LES results with moving waves show important differences compared with rough-wall boundary layers and flow over stationary bumps (i.e., hills). Bulk parameterizations of the surface drag need to account for wave state.

Acknowledgments. We thank Stephen Belcher, Edward Patton, and Anna Rutgersson who contributed to this work through several informal discussions. Bjorn Stevens and the anonymous reviewers provided critical comments and suggestions, which sharpened the text. Partial support for this work was provided by ONR Contracts N00014-00-C-0180 and N0001405IP20029 for P. Sullivan, ONR N00014-00-1-0409 and N00014-05-1-0139 for J. Edson, ONR N000140611017 for T. Hristov, and NSF DMS0327642 and ONR N00014-04-1-0166 for J. McWilliams.

APPENDIX

LES Model

a. LES equations in wave-following coordinates

An LES code with the capability of resolving a moving sinusoidal mode imposed at its lower boundary was developed. The computational approach is similar to that described in our direct numerical simulation (DNS) code (Sullivan and McWilliams 2002; Sullivan et al. 2000): first we translate the grid horizontally to take out the movement of the underlying surface and then we apply a grid transformation to the flow equations mapping the physical domain into a flat computational space (e.g., Anderson et al. 1984). As is standard computational practice, the mapping is applied only between Cartesian and computational coordinates $\mathbf{x_i} \rightarrow \xi_\mathbf{i}$. For the atmospheric PBL the working flow model is assumed to be unsteady, 3D, and described by incompressible Boussinesq equations with large-scale pressure gradients provided by geostrophic winds. The governing set of LES model equations in Cartesian coordinates for this flow is given by Moeng (1984). They include transport equations for resolved-scale (or spatially filtered) velocity $\overline{u}_i$ and virtual potential temperature $\overline{\theta}$:

$$\frac{\partial \overline{u}_i}{\partial t} = -\frac{\partial}{\partial x_j}(\overline{u}_j\overline{u}_i + \tau_{ij}) - \delta_{i3}\frac{g\overline{\theta}}{\theta_o} - \frac{\partial p^*}{\partial x_i} - \frac{1}{\rho_o}\frac{\partial \mathcal{P}}{\partial x_i} - \epsilon_{ijk}f_j\overline{u}_k \quad \text{and} \tag{A1a}$$

$$\frac{\partial \overline{\theta}}{\partial t} = -\frac{\partial}{\partial x_j}(\overline{u}_j\overline{\theta} + \psi_i), \tag{A1b}$$

with the velocity subject to the incompressibility constraint

$$\frac{\partial \overline{u}_i}{\partial x_i} = 0. \tag{A2}$$

In (A1) and (A2) spatially filtered variables are denoted by $\overline{(\;)}$. Other variables in (A1) include the rotation vector $\mathbf{f} = (0, 0, f)$ where f is the Coriolis parameter, gravity is g, the reference temperature and density are (θ_o, ρ_o), and the generalized pressure $p^* = \overline{p}/\rho_o + (2/3)e$, where $e = \tau_{ii}/2$ is the subgrid-scale energy. The large-scale externally imposed pressure gradients

$$-\frac{1}{\rho_o}\frac{\partial \mathcal{P}}{\partial x_i} = (-fV_g, fU_g, 0) \tag{A3}$$

are prescribed in terms of the x–y components of the geostrophic wind (U_g, V_g). The pressure p^* at each time step is the solution of a Poisson equation (Sullivan et al. 1996) formed from the discretized continuity Eq. (A2).

As a consequence of spatial filtering, subgrid-scale (SGS) fluxes of momentum $\tau_{ij} = \overline{u_i u_j} - \overline{u}_i\overline{u}_j - (2/3)\delta_{ij}e$ and its scalar $\psi_i = \overline{\theta u_i} - \overline{\theta}\,\overline{u}_i$ appear in (A1). In the present LES model these unknown fluxes are modeled using simple eddy viscosity prescriptions

$$\tau_{ij} = -\nu_t\left(\frac{\partial \overline{u}_i}{\partial x_j} + \frac{\partial \overline{u}_j}{\partial x_i}\right) \quad \text{and} \quad \psi_i = -\nu_t\left(1 + \frac{2l}{\Delta_f}\right)\frac{\partial \overline{\theta}}{\partial x_i}, \tag{A4}$$

with eddy viscosity $\nu_t = c_k l e^{1/2}$; c_k is a modeling constant and the length scale l is set equal to the LES filter Δ_f except in regions of stable stratification where it is reduced (Deardorff 1980). We note that SGS modeling is an active research area and numerous alternate approaches to modeling these SGS variables are available (e.g., Meneveau and Katz 2000; Geurts 2001; Sullivan et al. 2003; Wyngaard 2004; Sullivan et al. 2006a; Hatlee and Wyngaard 2007). LES solutions near flat parameterized z_o boundaries are dependent on the SGS closure (e.g., Mason and Thomson 1992; Sullivan et al. 1994; and others). This dependence is expected to be weaker in the present application as the surface form (pressure) stress is resolved. In other words there is less reliance on the SGS model to support surface fluxes in the presence of resolved wavy surfaces. This speculation is supported by direct numerical simulations Sullivan et al. (2000), but clearly requires further research.

The transport equation for subgrid-scale energy $e = \tau_{ii}/2$ is (Deardorff 1980)

$$\frac{\partial e}{\partial t} = -\frac{\partial}{\partial x_j}(\overline{u}_j e) - \frac{\tau_{ij}}{2}\left(\frac{\partial \overline{u}_i}{\partial x_j} + \frac{\partial \overline{u}_j}{\partial x_i}\right) + \frac{g}{\theta_o}\psi_3 + \frac{\partial}{\partial x_i}\left(2\nu_t \frac{\partial e}{\partial x_i}\right) - \mathcal{D} \tag{A5}$$

and includes, in order, time tendency, advection, SGS production, buoyancy, diffusion, and viscous dissipation. The latter is modeled using

$$\mathcal{D} = c_{\mathcal{D}} \frac{e^{3/2}}{\Delta_f}. \tag{A6}$$

The subgrid-scale constants $(c_k, c_{\mathcal{D}}) \approx (0.1, 0.93)$ (Moeng and Wyngaard 1988) are determined by applying a sharp cutoff filter in the inertial subrange and matching with a Kolmogorov spectrum.

The specific choice of grid transformation from physical to computational space relies on the problem definition. We assume the underlying wavy surface is an externally imposed, two-dimensional, single plane wave of height $h(x, t) = a\cos[k(x - ct)]$ with amplitude a, wavelength λ (or wavenumber $k = 2\pi/\lambda$) propagating with phase speed c. The wave is further assumed to obey the linear dispersion relationship $c^2 = g\lambda/2\pi$. As in second-order closure modeling (e.g., Gent and Taylor 1976) we introduce a streamwise coordinate $x' = x - ct$ to freeze the movement of the surface. The time and streamwise advective operators in (A1) for any field $\overline{g}$ then transform as

$$\frac{\partial \overline{g}}{\partial t} + \overline{u}\frac{\partial \overline{g}}{\partial x} \rightarrow \frac{\partial \overline{g}}{\partial t} + (\overline{u} - c)\frac{\partial \overline{g}}{\partial x'}. \tag{A7}$$

Allowing the grid to advect horizontally with translation speed c is equivalent to applying a Galilean transformation to the governing equations: the model equations are not fundamentally changed if we replace $\overline{u}$ *by* $\overline{u}' = \overline{u} - c$. Next, the physical space coordinates (x', y, z) are mapped to computational coordinates $\boldsymbol{\xi} \equiv \xi_i = (\xi, \eta, \zeta)$ using the grid transformation

$$\xi = \xi(x', z), \quad \eta = y, \quad \zeta = \zeta(x', z), \tag{A8}$$

with the Jacobian of the transformation $J = \xi_x\zeta_z - \xi_z\zeta_x$. In transforming the flow equations, described below, we frequently make use of the grid transformation identity (Anderson et al. 1984)

$$\frac{\partial}{\partial \xi_j}\left(\frac{\partial \xi_j}{\partial x_i}\frac{1}{J}\right) = 0 \quad \text{for} \quad i = 1, 2, 3. \tag{A9}$$

In anticipation of the numerical solution of (A1) and (A2) we introduce contravariant flux velocities

$$U = \frac{\overline{u}\xi_x + \overline{w}\xi_z}{J}, \quad V = \frac{\overline{v}}{J}, \quad \text{and} \quad W = \frac{\overline{u}\zeta_x + \overline{w}\zeta_z}{J}, \tag{A10}$$

which point in directions perpendicular to the computational cell faces (η–ζ, ξ–ζ, ξ–η), respectively. They satisfy the transformed continuity equation

$$\frac{\partial \overline{u}_i}{\partial x_i} \equiv \frac{\partial U_i}{\partial \xi_i} = 0. \tag{A11}$$

Applying the grid transformation (A8) to (A1) and (A5), and making use of the continuity Eq. (A11) and the identity (A9) yields the transformed set of LES equations in strong conservation form:

$$\frac{\partial \overline{u}_i}{\partial t} = -J\frac{\partial}{\partial \xi_j}(U_j\overline{u}_i) - \delta_{i3}\frac{\partial \overline{\theta}}{\theta_o} - \frac{1}{\rho_o}\frac{\partial \mathcal{P}}{\partial x_i} - \epsilon_{ijk}f_j\overline{u}_k - J\frac{\partial}{\partial \xi_j}\left(\frac{\partial \xi_j}{\partial x_i}\frac{p^*}{J}\right) - J\frac{\partial}{\partial \xi_j}\left(\frac{\partial \xi_j}{\partial x_k}\frac{\tau_{ik}}{J}\right), \tag{A12a}$$

$$\frac{\partial \overline{\theta}}{\partial t} = -J\frac{\partial}{\partial \xi_j}(U_j\overline{\theta}) - J\frac{\partial}{\partial \xi_j}\left(\frac{\partial \xi_j}{\partial x_i}\frac{\psi_i}{J}\right), \quad \text{and} \tag{A12b}$$

$$\frac{\partial e}{\partial t} = -J\frac{\partial}{\partial \xi_j}(U_j e) + \frac{g}{\theta_o}\psi_3 - \mathcal{D} - \frac{\tau_{ij}}{2}\left(\frac{\partial \overline{u}_i}{\partial \xi_k}\frac{\partial \xi_k}{\partial x_j} + \frac{\partial \overline{u}_j}{\partial \xi_k}\frac{\partial \xi_k}{\partial x_i}\right) + J\frac{\partial}{\partial \xi_k}\left[\frac{\partial \xi_k}{\partial x_i}\frac{2\nu_t}{J}\left(\frac{\partial \xi_j}{\partial x_i}\frac{\partial e}{\partial \xi_j}\right)\right]. \tag{A12c}$$

b. Boundary conditions

The flow is assumed to be homogeneous in horizontal planes and thus explicit boundary conditions only need to be specified at the water surface and at the top of the computational domain. The upper boundary in physical space is located far above the wavy surface and as a result the horizontal gridlines are flat and orthogonal to vertical grid lines. At the top of the computational domain the upper boundary conditions are simply set equal to the values in our flat LES code. We use a radiation condition (Klemp and Durran 1983) for vertical velocity along with a specified constant gradient for potential temperature, zero vertical gradients for the horizontal velocities, and zero SGS turbulence fields (Moeng 1984).

The important changes occur at the lower boundary $z = z_b = h(x, t)$ where the Cartesian velocity components are set equal to the orbital velocity of the resolved wave $(\overline{u}, \overline{w})_s = akc\{\cos[k(x - ct)], \sin[k(x - ct)]\}$

[e.g., section 3.2 of Lighthill (1978)]. In the frame of reference moving with speed c the boundary conditions on the Cartesian velocity components are

$$\begin{bmatrix} \overline{u}' \\ \overline{v} \\ \overline{w} \end{bmatrix} = \begin{bmatrix} -c + \overline{u}_s \\ 0 \\ \overline{w}_s \end{bmatrix}, \tag{A13}$$

which requires the contravariant flux velocities satisfy

$$\begin{bmatrix} JU \\ JV \\ JW \end{bmatrix} = \begin{bmatrix} (-c + \overline{u}_s)\xi_x + \overline{w}_s\zeta_x \\ 0 \\ (-c + \overline{u}_s)\xi_z + \overline{w}_s\zeta_z \end{bmatrix}. \tag{A14}$$

For a sinusoidal waveform of small wave slope $ak \ll 1$ the boundary conditions on the contravariant flux velocities become $J(U, V, W) \rightarrow (-c, 0, 0)$ (Sullivan et al. 2000).

A key difference between the LES and DNS is the formulation of the boundary condition on surface fluxes. The LES is intended to model a high Reynolds number geophysical flow and in this regime it is not computationally feasible to resolve the viscous sublayer. Therefore we apply bulk drag formulas to estimate subgrid-scale surface fluxes of momentum and scalars, similar to the approach in an LES with a flat boundary. The total drag on the PBL consists of resolved form stress and an unresolved viscous drag that rides on the wavy surface. In the LES, a high-Reynolds number surface drag law based on a "z_o" boundary condition is adopted at the lower boundary, essentially a law-of-the-wall expression is applied instantaneously at every surface grid point to relate the surface winds and fluxes. Mason and Callen (1986) and Wyngaard et al. (1998) discuss the applicability of this approximation, which is experimentally verified in a flat plate boundary layer flow by Nakayama et al. (2004). We adapt this law-of-the-wall parameterization to our wavy-surface application, similar to the methodology used in second-order closure modeling (Gent and Taylor 1976; Li 1995). In a neutrally stratified flow, the surface friction velocity u_* due to the unresolved surface waves (or roughness) is estimated from

$$|\mathbf{U}_{\|}(\Delta\zeta/2)| = \frac{u_*}{k} \ln\left(\frac{\Delta\zeta/2}{z_o}\right), \tag{A15}$$

where $\kappa = 0.4$ is the von Kármán constant, z_o is the specified surface roughness, and $\Delta\zeta = \zeta_1 - h$ is the normal distance from the surface wave h to the first ζ grid point; $\mathbf{U}_{\|} = (\mathbf{u} \cdot \mathbf{s})$, where $\mathbf{s}$ and $|\mathbf{U}_{\|}|$ are the wind vector and wind speed parallel to the surface, with $\mathbf{s}$ the unit vector tangent to the surface. The surface momentum flux τ estimated from the bulk formula

$$\boldsymbol{\tau} = C_D|\mathbf{U}_{\|}|\mathbf{U}_{\|}, \quad \text{with} \quad C_D = \left\{\frac{\kappa}{\ln[(\Delta\zeta/2)/z_o]}\right\}^2 \tag{A16}$$

assumes the surface stress and the surface wind are parallel. In PBL flows with surface heating or cooling a constant surface buoyancy flux is specified, and u_* is modified using Monin–Obukhov similarity functions (Moeng 1984). This correction is small in the present application since the first vertical grid level is quite close to the surface, $\Delta\zeta_1 \approx 1$ m. The wave-following surface stresses $\boldsymbol{\tau}$ are the physical components of a second-order tensor and are converted into the Cartesian stress τ_{ij}, needed in (A12), using standard transformation rules (see section 13.3 of Wylie 1966).

c. Numerical method and grid generation

The numerical algorithm used to integrate the LES model Eqs. (A11) and (A12) is identical to that in our DNS code (Sullivan and McWilliams 2002; Sullivan et al. 2000). For our mixed finite-difference pseudospectral differencing scheme a special arrangement of variables is employed. The Cartesian velocity and scalar variables $(\overline{\mathbf{u}}, \overline{\theta}, p^*, e)$ are colocated at cell centers while the contravariant flux velocities (U, V) are located at cell centers with W located at cell faces. The positioning of U_i mimics the arrangement of variables in our flat Cartesian LES code. Advantages of the colocated grid structure are as follows: 1) all advective terms can be compactly discretized using a skew symmetric form, namely, $[\partial(U_j\overline{u}_i)/\partial\xi_j + U_j\partial\overline{u}_i/\partial\xi_j]/2$ for momentum advection and $[\partial(U_j\overline{\theta})/\partial\xi_j + U_j\partial\overline{\theta}/\partial\xi_j]/2$ for scalar advection; and 2) the location and orientation of U maintains tight velocity–pressure coupling as the continuity equation $\partial U_i/\partial\xi_i$ is used to construct the discrete pressure Poisson equation. The spatial discretization is pseudospectral along lines of constant ξ or η and second-order finite difference in the vertical coordinate ζ. A third-order Runge–Kutta time-stepping scheme operating with a fixed CFL number is employed (Sullivan et al. 1996). An important difference from a flat Cartesian code is the appearance of variable coefficients in the pressure Poisson equation. This prevents a direct solution using Fourier transforms and tridiagonal matrix inversion for each pair of horizontal wavenumbers. Here we use an iterative solution method for the pressure described in Sullivan et al. (2000). The entire code is parallelized using the Message Passing Interface (MPI) with domain decomposition in ζ. A custom-built MPI matrix transpose is used in the solution of the pressure Poisson equation.

The final element in our computational procedure is the generation of an acceptable field grid. Since the underlying waveform is simple and stationary in computational space an adequate mesh can be created using conformal techniques. Given periodicity in the horizontal direction, a flat upper boundary, and a specified surface wave, we then solve two standard elliptic grid generation equations for the (x', z) coordinates (Thompson et al. 1985; Dimitropoulos et al. 1998):

$$\frac{\partial^2 x'}{\partial \xi^2} + \frac{\partial^2 x'}{\partial \zeta^2} = 0 \quad \text{and} \quad \frac{\partial^2 z}{\partial \xi^2} + \frac{\partial^2 z}{\partial \zeta^2} = 0. \tag{A17}$$

The vertical boundary conditions at the surface $\zeta = 0$ and at the top of the computational domain $\zeta = z_L$ are

$$z = h(x'), \quad \frac{\partial x'}{\partial \zeta} = -\frac{\partial h}{\partial x'}\frac{\partial z}{\partial \zeta} \quad \text{at} \quad \zeta = 0 \quad \text{and} \tag{A18a}$$

$$z = z_L, \quad \frac{\partial x'}{\partial \zeta} = 0 \quad \text{at} \quad \zeta = z_L. \tag{A18b}$$

The numerical solution of these elliptic equations generates smoothly varying grids. The grid metrics and Jacobian are constructed numerically from the one-to-one mapping between (x', y, z) and (ξ, η, ζ). We note the use of a conformal grid is quite advantageous in DNS as it greatly streamlines the viscous term, but does not lead to the same simplification in LES since the subgrid flux terms contain spatially varying eddy viscosity and diffusivity. Last, in order to focus the grid near the surface the vertical spacing is varied using constant algebraic stretching; that is, the ratio of any two adjacent vertical cells is held constant, $K = \Delta\zeta_{i+1}/\Delta\zeta_i$. Stretching factors $K \leq 1.036$ vary the grid smoothly but at the same time provide adequate leverage to span a large vertical extent.

REFERENCES

Adrian, R. J., and Z. C. Liu, 2002: Observation of vortex packets in direct numerical simulation of fully turbulent channel flow. *J. Visualization,* **5,** 9–19.

Alves, J. H. G. M., M. L. Banner, and I. R. Young, 2003: Revisiting the Pierson–Moskowitz asymptotic limits for fully developed wind waves. *J. Phys. Oceanogr.,* **33,** 1301–1323.

Anderson, D. A., J. C. Tannehill, and R. H. Pletcher, 1984: *Computational Fluid Mechanics and Heat Transfer.* McGraw-Hill, 599 pp.

Beare, R. J., and Coauthors, 2006: An intercomparison of large-eddy simulations of the stable boundary layer. *Bound.-Layer Meteor.,* **118,** 247–272.

Belcher, S. E., and J. C. R. Hunt, 1998: Turbulent flow over hills and waves. *Annu. Rev. Fluid Mech.,* **30,** 507–538.

Chambers, A. J., and R. A. Antonia, 1981: Wave-induced effect on the Reynolds shear stress and heat flux in the marine surface layer. *J. Phys. Oceanogr.,* **11,** 116–121.

Churchill, J. H., A. J. Plueddemann, and S. M. Faluotico, 2006: Extracting wind sea and swell from directional wave spectra derived from a bottom-mounted ADCP. Woods Hole Oceanographic Institution Tech. Rep. WHOI-2006-13, 41 pp.

Cohen, J. E., and S. E. Belcher, 1999: Turbulent shear flow over fast-moving waves. *J. Fluid Mech.,* **386,** 345–371.

Deardorff, J. W., 1980: Stratocumulus-capped mixed layers derived from a three-dimensional model. *Bound.-Layer Meteor.,* **18,** 495–527.

Dimitropoulos, C. D., B. J. Edwards, K.-S. Chae, and A. N. Beris, 1998: Efficient pseudospectral flow simulations in moderately complex geometries. *J. Comput. Phys.,* **144,** 517–549.

Donelan, M. A., 1998: Air-water exchange processes. *Physical Processes in Lakes and Oceans,* J. Imberger, Ed., Vol. 54, Coastal and Estuarine Studies, Amer. Geophys. Union, 19–36.

——, and W. J. Pierson, 1987: Radar scattering and equilibrium ranges in wind-generated waves with application to scatterometry. *J. Geophys. Res.,* **92,** 4971–5029.

——, W. M. Drennan, and K. B. Katsaros, 1997: The air–sea momentum flux in conditions of wind sea and swell. *J. Phys. Oceanogr.,* **27,** 2087–2099.

Drennan, W. M., K. K. Kahma, and M. A. Donelan, 1999: On momentum flux and velocity spectra over waves. *Bound.-Layer Meteor.,* **92,** 489–515.

Edson, J., C. W. Fairall, and P. P. Sullivan, 2006: Evaluation and continued improvements to the TOGA COARE 3.0 bulk flux algorithm using CBLAST data. Preprints, *27th Conf. on Hurricanes and Tropical Meteorology,* Monterey, CA, Amer. Meteor. Soc., 7C.1. [Available online at http://ams.confex.com/ams/pdfpapers/108533.pdf.]

——, and Coauthors, 2007: The coupled boundary layers and air–sea transfer experiment in low winds. *Bull. Amer. Meteor. Soc.,* **88,** 341–356.

Fairall, C. W., E. F. Bradley, J. E. Hare, A. A. Grachev, and J. B. Edson, 2003: Bulk parameterization of air–sea fluxes: Updates and verification for the COARE algorithm. *J. Climate,* **16,** 571–591.

Garratt, J. R., 1992: *The Atmospheric Boundary Layer.* Cambridge University Press, 316 pp.

Gent, P. R., 1977: A numerical model of the air flow above water waves. Part 2. *J. Fluid Mech.,* **82,** 349–369.

——, and P. A. Taylor, 1976: A numerical model of the air flow above water waves. *J. Fluid Mech.,* **77,** 105–128.

Geurts, B. J., Ed., 2001: *Modern Simulation Strategies for Turbulent Flow.* R. T. Edwards, 327 pp.

Grachev, A. A., and C. W. Fairall, 2001: Upward momentum transfer in the marine boundary layer. *J. Phys. Oceanogr.,* **31,** 1698–1711.

——, ——, J. E. Hare, J. B. Edson, and S. D. Miller, 2003: Wind stress vector over ocean waves. *J. Phys. Oceanogr.,* **33,** 2408–2429.

Hanson, J. L., and O. M. Phillips, 2001: Automated analysis of ocean surface directional wave spectra. *J. Atmos. Oceanic Technol.,* **18,** 277–293.

Harris, D. L., 1966: The wave-driven wind. *J. Atmos. Sci.,* **23,** 688–693.

Hatlee, S. C., and J. C. Wyngaard, 2007: Improved subfilter-scale models from the HATS field data. *J. Atmos. Sci.,* **64,** 1694–1705.

Holland, J. Z., W. Chen, J. A. Almazan, and F. C. Elder, 1981: Atmospheric boundary layer. *IFYGL—The International Field Year for the Great Lakes,* E. J. Aubert and T. L. Richards, Eds., NOAA–GLERL, U.S. Dept. of Commerce, 109–167.

Hommema, S. E., and R. J. Adrian, 2003: Packet structure of surface eddies in the atmospheric boundary layer. *Bound.-Layer Meteor.,* **106,** 147–170.

Klemp, J. B., and D. R. Durran, 1983: An upper boundary condition permitting internal gravity wave radiation in numerical mesoscale models. *Mon. Wea. Rev.,* **111,** 430–444.

Komen, G. J., L. Cavaleri, M. Donelan, K. Hasselmann, S. Hasselmann, and P. A. E. M. Janssen, 1994: *Dynamics and Modelling of Ocean Waves.* Cambridge University Press, 532 pp.

Kudryavtsev, V. N., and V. K. Makin, 2004: Impact of swell on the marine atmospheric boundary layer. *J. Phys. Oceanogr.,* **34,** 934–949.

Li, P. Y., 1995: A numerical study on energy transfer between turbulent air flow and finite amplitude water waves. Ph.D. thesis, York University, 181 pp.

Lighthill, M. J., 1978: *Waves in Fluids.* Cambridge University Press, 504 pp.

Lin, C.-L., J. C. McWilliams, C.-H. Moeng, and P. P. Sullivan, 1996: Coherent structures and dynamics in a neutrally stratified planetary boundary layer flow. *Phys. Fluids,* **8,** 2626–2639.

Makin, V. K., and C. Mastenbroek, 1996: Impact of waves on air-sea exchange of sensible heat and momentum. *Bound.-Layer Meteor.,* **79,** 279–300.

Mason, P. J., and N. S. Callen, 1986: On the magnitude of the subgrid-scale eddy coefficient in large-eddy simulations of turbulent channel flow. *J. Fluid Mech.,* **162,** 439–462.

——, and D. J. Thomson, 1992: Stochastic backscatter in large-eddy simulations of boundary layers. *J. Fluid Mech.,* **242,** 51–78.

Meneveau, C., and J. Katz, 2000: Scale-invariance and turbulence models for large-eddy simulation. *Annu. Rev. Fluid Mech.,* **32,** 1–32.

Miller, S. D., 1999: The structure of turbulent and wave-induced wind fields over open-ocean waves. Ph.D. thesis, University of California, Irvine, 221 pp.

Moeng, C.-H., 1984: A large-eddy-simulation model for the study of planetary boundary-layer turbulence. *J. Atmos. Sci.,* **41,** 2052–2062.

——, and J. C. Wyngaard, 1988: Spectral analysis of large-eddy simulations of the convective boundary layer. *J. Atmos. Sci.,* **45,** 3573–3587.

——, and ——, 1989: Evaluation of turbulent transport and dissipation closures in second-order modeling. *J. Atmos. Sci.,* **46,** 2311–2330.

——, and P. P. Sullivan, 1994: A comparison of shear- and buoyancy-driven planetary boundary layer flows. *J. Atmos. Sci.,* **51,** 999–1022.

Nakayama, A., H. Noda, and K. Maeda, 2004: Similarity of instantaneous and filtered velocity fields in the near wall region of zero-pressure gradient boundary layer. *Fluid Dyn. Res.,* **35,** 299–321.

Plant, W. J., 1982: A relationship between wind stress and wave slope. *J. Geophys. Res.,* **87,** 1961–1967.

Rutgersson, A., A.-S. Smedman, and U. Högström, 2001: Use of conventional stability parameters during swell. *J. Geophys. Res.,* **106,** 27 117–27 134.

Saiki, E. M., C.-H. Moeng, and P. P. Sullivan, 2000: Large-eddy simulation of the stably stratified planetary boundary layer. *Bound.-Layer Meteor.,* **95,** 1–30.

Scotti, A., C. Meneveau, and D. K. Lilly, 1993: Generalized Smagorinsky model for anisotropic grids. *Phys. Fluids A,* **5,** 2306–2308.

Smedman, A.-S., M. Tjernström, and U. Högström, 1994: The near-neutral marine atmospheric boundary layer with no surface shearing stress: A case study. *J. Atmos. Sci.,* **51,** 3399–3411.

——, U. Högström, and H. Bergström, 1997: The turbulence regime of a very stable marine airflow with quasi-frictional decoupling. *J. Geophys. Res.,* **102,** 21 049–21 060.

——, ——, ——, A. Rutgersson, K. K. Kahma, and H. Pettersson, 1999: A case study of air-sea interaction during swell conditions. *J. Geophys. Res.,* **104,** 25 833–25 852.

——, ——, and A. Sjöblom, 2003: A note on velocity spectra in the marine boundary layer. *Bound.-Layer Meteor.,* **109,** 27–48.

Sullivan, P. P., and J. C. McWilliams, 2002: Turbulent flow over water waves in the presence of stratification. *Phys. Fluids,* **14,** 1182–1195.

——, ——, and C.-H. Moeng, 1994: A subgrid-scale model for large-eddy simulation of planetary boundary-layer flows. *Bound.-Layer Meteor.,* **71,** 247–276.

——, ——, and ——, 1996: A grid nesting method for large-eddy simulation of planetary boundary-layer flows. *Bound.-Layer Meteor.,* **80,** 167–202.

——, ——, and ——, 2000: Simulation of turbulent flow over idealized water waves. *J. Fluid Mech.,* **404,** 47–85.

——, T. W. Horst, D. H. Lenschow, C.-H. Moeng, and J. C. Weil, 2003: Structure of subfilter-scale fluxes in the atmospheric surface layer with application to large-eddy simulation modelling. *J. Fluid Mech.,* **482,** 101–139.

——, J. B. Edson, J. C. McWilliams, and C.-H. Moeng, 2004: Large-eddy simulations and observations of wave-driven boundary layers. Preprints, *16th Symp. on Boundary Layers and Turbulence,* Portland, ME, Amer. Meteor. Soc., 8.12. [Available online at http://ams.confex.com/ams/pdfpapers/78119.pdf.]

——, ——, T. W. Horst, J. C. Wyngaard, and M. Kelly, 2006a: Subfilter scale fluxes in the marine surface layer: Results from the Ocean Horizontal Array Turbulence Study (OHATS). Preprints, *17th Symp. on Boundary Layers and Turbulence,* San Diego, CA, Amer. Meteor. Soc., 4.1.

——, ——, T. Hristov, and J. C. McWilliams, 2006b: Momentum flux structures and statistics in low-wind marine surface layers: Observations and large-eddy simulations. Preprints, *27th Conf. on Hurricanes and Tropical Meteorology,* Monterey, CA, Amer. Meteor. Soc., 7C.6. [Available online at http://ams.confex.com/ams/pdfpapers/110884.pdf.]

Thompson, J. F., Z. U. A. Warsi, and C. W. Mastin, 1985: *Numerical Grid Generation: Foundations and Applications.* North-Holland, 483 pp.

Wylie, C. R., 1966: *Advanced Engineering Mathematics.* 3rd ed. McGraw-Hill, 813 pp.

Wyngaard, J. C., 2004: Toward numerical modeling in the “terra incognita.” *J. Atmos. Sci.,* **61,** 1816–1826.

——, L. J. Peltier, and S. Khanna, 1998: LES in the surface layer: Surface fluxes, scaling, and SGS modeling. *J. Atmos. Sci.,* **55,** 1733–1754.